POLITECNICO
MILANO 1863

SCUOLA DI INGEGNERIA INDUSTRIALE
E DELL'INFORMAZIONE

IMU-based upper limb kinematics: from exosuit control to motor primitives classification

Tesi di Laurea Magistrale in
Biomedical Engineering - Ingegneria Biomedica

Carola Butera, 953592

Abstract: In the presence of a chronic upper limb (UL) impairment, the quality of life of the person affected can be severely compromised. For this reason, motor rehabilitation and assistance with activities of daily living (ADLs) are fundamental. In the context of home assistance, exoskeletons represent a valid tool to assist UL movements in the execution of ADLs thanks to cooperation between sensors and actuators. This thesis is part of a project aimed at the development of a cable-driven exosuit for upper-limb assistance. Three inertial measurement units (IMUs) are integrated into the device to allow real-time gravity compensation. The vision behind this work is to exploit these sensors to build a kinematic model of the UL to accomplish exosuit control and evaluate daily the user's UL functionality progress to provide feedback and promote user engagement. To this aim, two objectives were defined: i) implementing the online computation of anatomical angles in accordance with the ISB (International Society of Biomechanics) standard, ii) defining, training, and testing a neural network for motor primitives classification. To achieve the first objective, a 3-step (IMU reset, N-pose and T-pose) calibration procedure was proposed. Then, the formalization of the computation method for 5 ISB angles including plane of elevation (POE), angle of elevation (AOE), humeral rotation (HR), flexion/extension (FE), and pronation/supination (PS),, was completed. The method was validated on a robotic arm and on 5 healthy participants by means of comparison between the IMUs and the robot's encoders and an optoelectronic system respectively. For the second objective, 10 healthy participants were asked to execute a set of activities in two different settings: one characterized by simple ADLs (SADL) and the other by more complex ADLs (CADL). During the experiments, data were acquired by means of 5 IMUs and a video camera to provide ground truth for the labeling process. Data were labeled by means of video inspection according to the definition of 5 motor primitives: 'idle', 'stabilize', 'reach, 'transport', and 'reposition'. A Long-Short Term Memory (LSTM) neural network was then trained and tested with different combinations of datasets: SADL for both training and test and SADL+CADL for both training and test. Results of the validation on ISB angles showed a lower error during the test on the robotic arm (mean RMSE 2.75°-4.96°) with respect to that on participants (mean RMSE 9.45°-29.65°). Nevertheless, the correlation coefficient was greater than 0.91 also during the validation with healthy subjects. For what concerns the classification performance of the LSTM model on the 2 datasets, the first achieved an f1-score of 0.75, while the second, which is more relevant for the final application, obtained an f1-score of 0.73. The algorithm performed better in the estimation of 'idle' and 'transport' primitives, which were the most present in the datasets. On the contrary, 'reach' and 'reposition' primitives were often misclassified as 'transport'. This work represents a starting point for UL assessment in daily living scenarios.

Advisor:
Prof. Emilia Ambrosini

Co-advisors:
Elena Bardi

Academic year:
2022-2023

Key-words: upper limb kinematics, exosuit control, IMU joint angles computation, ISB standard, motor primitives classification, neural networks

1. Introduction

1.1. Clinical problem

Upper limb motor impairment is a condition that can occur both due to neurological and neuromuscular disorders, such as stroke and muscular dystrophy, and as a consequence of traumatic events that have severely injured the spinal cord. During the acute phase, stroke leads to upper limb (UL) impairment in the 80% of the affected subjects, 65% of which report a chronic loss of functionality afterward [1]. Upper extremity motor impairment can arise at the muscle level as a loss of strength or ability to control muscle contraction [2] making the execution of basic activities in everyday life challenging.
The constant need for assistance in the execution of activities of daily living (ADLs) as a consequence of chronic arm impairment contributes to a loss of independence which can lead to a decrease in the individual's participation in usual activities, ultimately resulting in a deterioration of the quality of life [3]. Impaired subjects might develop compensatory strategies which can be observed at the neural level as a different activation of brain areas compared to the period preceding the injury. Moreover, they can appear in alternative movement patterns like unnatural muscles activation of the damaged arm or learned avoidance of its use [3]. Learned non-use is observable in an increase of unaffected limb use, particularly evident in the execution of unimanual tasks, and in a lowered movement intensity of the impaired arm which can be observed during bimanual activities [4].
To mitigate the consequences of motor impairment, rehabilitation is fundamental. In the case of stroke or spinal cord injury, the most common treatment approach of UL-impaired patients is to perform in clinical settings sessions of exercises and functionality assessments which are planned in a specific schedule within the first 6 months since the occurrence of the ischemic/hemorrhagic event or the spinal trauma. Specialized practitioners guide rehabilitative exercises which consist in the repetition of well-defined movements. The positive effects of an extension of the rehabilitation program during the chronic stage have been proved [5], but the limited resources of clinical centers reduce the feasibility of prolonging the rehabilitation treatment after the customary period.
During rehabilitation sessions, the evaluation of the functionality of the UL is commonly carried out through the application of standard clinical scales like Fugl Meyer Assessment for Upper Extremity (FMA-UE) and Action Research Arm Test (ARAT) to assess the patient's improvements and to personalize the treatment. The application of FMA, ARAT, or similar clinical scales involves the conduction of several tests by the clinician: assessment through clinical scale is therefore time-consuming [6], and due to the limited available time for each session, can take up time for training reducing the efficacy of the treatment.
In this context, the clinical approach to rehabilitation and assessment has limitations that need to be considered: the presence of limited resources, namely the availability of therapists, coupled with an increase in demand as a result of the world's population aging, may lead to an under-treatment of patients. Moreover, the rehabilitation path may not be optimal for the patient as the accuracy of progress assessments can be compromised due to the presence of the above-mentioned compensatory strategies, which are not always recognizable [**?**]. Moreover, factors like patient engagement and practitioner subjectivity may influence the assessment [7].
Recent studies have underlined the advantages of using wearable sensors that can provide measurements of the kinematics of the upper limb that can be used to perform an objective assessment of the patient's recovery. Among the potential advantages provided by wearable sensors, one of these is the possibility to provide continuous arm movement registration: a more consistent and meaningful evaluation of movement can be achieved which in turn can result in a better understanding of functional progress. The application of wearable technologies extends beyond movement evaluation: the kinematic and dynamic measures provided by wearable sensors, like inertial measurement units (IMUs), can be exploited in assistive robot control. The ongoing research on robotic exoskeletons is playing a substantial role in the innovation of the rehabilitation journey, both in the clinical settings, to increase treatment dose intensity [8], and in-home environments as assistive devices.
This thesis falls within a project conducted at Politecnico di Milano which is focused on the development of a soft exoskeleton for the daily assistance of UL movements. This device is designed to assist patients in the execution of activities of daily living outside of the clinical environment with the objective to restore the individual's independence and improve his quality of life. The primary function of this exoskeleton is the compensation of arm weight against gravity, which is achieved through a real-time control based on the data acquired by three IMUs placed on the thorax, impaired upper arm, and impaired forearm. The underlying motivation of this thesis is to leverage the large amount of data obtained from sensors that are already embedded in the exosuit,

which can therefore be useful for control and assessment purposes. The direction towards which this research is aimed is the development of a system capable of assisting the impaired arm movement in daily living and assessing upper arm use to generate a daily report which is descriptive of the trend of UL progress. The idea is that this report could be accessible both to the practitioner, who can remotely and continuously monitor progresses, and to the patient. Delivering the report to the patient can be an effective tool to enhance his engagement in the daily use of the exoskeleton: a research study [9] has shown that feedback plays a crucial role in motivating patients to engage with assistive devices, thereby promoting movement and facilitating the use of technology in their daily lives.
In the following section, a brief overview of the state of the art of assistive robotics, movement classification, and assessment will be presented to provide a clear context for this study.

1.2. Rehabilitation and assistive robotics

The ongoing research in novel techniques for rehabilitation and assistive technologies is bustling in the direction of robotic devices. Different studies [8] have underlined benefits arising from the introduction of this kind of approach in the clinical and home scenario, thanks to the repeatability and precision that this technology can offer. Exoskeletons are devices popular in the neurorehabilitation and robotic assistance field [10]. These devices are wearable and composed of rigid segments linked to each other and aligned to the body segments whose movements can be controlled by the synergic action of sensors and actuators. Exoskeletons have been developed both for upper limbs and lower limbs.
Wearable robotic devices, better known as UL exoskeletons, have been developed for different purposes: augmentation, rehabilitation, and assistance [11], [12]. Technologies for augmenting functions have been mainly implemented in the industrial field, for example, to provide assistance to warehouse workers in lifting heavy weights and reduce injury risks associated with this activity. In the rehabilitation scenario, the use of rigid exoskeletons can bring several advantages both for the patient and the specialized practitioner: session efficacy can be improved in terms of an increase in exercise dose [13] and precision of movement assessment [14]. The presence of sensors, like encoders, which are embedded in the robotic structure for control purposes, facilitates the extraction of objective measurements allowing high accuracy in tracking trajectories and in the estimation of kinematic metrics like the Range Of Motion (ROM), accelerations, and velocities. Despite the popularity of rigid exoskeletons in industrial and clinical applications, in-home rehabilitation or in the assistive scenario, these devices may not be the best choice: their structure, mainly composed of stiff materials like metal and plastic, could be weighty and the rigid configuration may hamper the freedom of movement of the arm. The need to perform laborsome alignment between rigid robot links and body segments entails that wearing them requires external assistance from a specialized practitioner [15].
For these reasons, recent studies have been focusing on the development of a novel generation of assistive exoskeletons, also known as exosuits, which are mainly composed of soft materials. The idea behind this kind of devices is to get rid of the bulky structure in favor of textile interfaces which are lightweight, more comfortable, and ensure higher compliance between the device and the user. Due to their soft structures, these technologies can exert lower torques with respect to rigid ones but the lack of rigid joints makes for an ease of wearing thus avoiding laborsome alignment procedures [12]. Moreover, the movements enabled by soft exoskeletons are more fluid and less constrained than the rigid ones. A significant advantage is also the reduction of costs introduced by the use of affordable materials: exosuits represent a more cost-effective technology that could be more easily widely distributed. In terms of actuation, soft exosuits can be driven by cables [16] or use pneumatic [17] or passive forces [18]. Cable-driven soft exoskeletons, also called tensile exosuits, are the most explored ones nowadays. They are characterized by the use of tendons, which are connected to various anchoring points on the exoskeleton, and that can transmit the force exerted by the motor which in turn can be placed distantly from the point at which the force is intended to be applied. This characteristic allows the installation of actuators, batteries and other elements necessary for the control of the exosuit in a non-obtrusive positioning.

1.3. UL function assessment and movement classification

1.3.1 Clinical assessment

Movement evaluation in neurorehabilitation is usually performed through the application of clinical scales. The most popular scales used for upper limb assessment are the Fugl-Meyer Assessment (FMA) scale [6] and the Action Arm Research Test [19]. The former, considered a gold standard for the upper and lower limb, consists of a standardized sensorimotor evaluation of the extremity's motor function, sensation, pain, balance, and joint range of motion. This standard was primarily developed for patients with hemiplegia caused by stroke. During the execution of FMA-UE (FMA for Upper Extremity), the patient is instructed to perform a series of well-defined tasks: an example is to move the hand from the contralateral knee to the ipsilateral ear. The target of

the evaluation is the upper extremity, wrist, and hand movement quality as well as their coordination, reflexes activity, and speed. The outcome of this standardized evaluation is a numerical score that depicts the level of overall severity of the arm motor impairment and is computed by summing up the scores assigned to every single task. The latter clinical scale, the ARAT test, differently from FMA-UE, aims to the evaluation of UL performance in tasks belonging to daily activities such as reaching, grasping, and object manipulation. This evaluation protocol includes 19 items comprising grasp, grip, pinch, and gross movement movements that are evaluated with a score between 0 and 3.
Despite the popularity of these clinical scales, they present several drawbacks such as floor and ceiling effects [20]. Moreover, as they rely on observational measures, the personal interpretation of the test administrator can affect the objectivity and reliability of the measure thus bringing in inter-rater and intra-rater variability. The scoring method also introduces a lack of specificity, in particular in the assessment of mildly impaired subjects [21]. The evaluation of movements could also be over-estimated by the arising of compensatory strategies, like the introduction of trunk compensation, which are not always easily discernible by the eye of the practitioner [**?**]. These limitations in the use of clinical scales, combined with healthcare systems' difficulty in complying with an increasing number of requests to provide an adequate frequency in monitoring progress, steered the research to the integration of sensors in clinical assessment.

1.3.2 Sensor-based UL assessment

The analysis of arm kinematics, which involves the study of positions, velocities, and accelerations, can be integrated with the use of clinical scales having the advantage to provide objective analysis. Indeed, sensors are widely used for motion capture, especially in lower limb applications like gait analysis following surgical intervention [22]. Moreover, with rehabilitation exoskeletons, it is possible to monitor the patient during exercise execution: one way is to record electromyographic signal by means of the sensors embedded in the exoskeleton [23]. Among the technologies that can perform an objective assessment of arm use, accelerometers represent a reliable tool both for their applicability in home settings and precision of measurements [24].
The first and most intuitive metric that can be extracted from accelerometers is Activity counts (AC) [25]. AC is an easily measurable metric based on the data acquired by a uniaxial accelerometer. The sum of the raw linear acceleration is usually computed over a few seconds windows [26]. If the value of the sum of the accelerations evaluated in a specific epoch overcomes a threshold, the window is tagged as a "movement", otherwise as "non-movement". The overall number of windows labeled as "movement" obtained through the analysis of the accelerations acquired during a long period of time (24 hours in the cited study), provides a description of the amount of upper arm use. Despite the ease of application, this metric brings along a main drawback: the passive movements involved in activities like walking, in which the arms are swung unintentionally, may be recognized as activity leading to overestimation of the activity count [27]. The correlation of activity counts with clinical scales is, in fact, low [28].
Bayley et al. [27] proposed an alternative application of the activity count by registering the accelerations of both paretic and non-paretic arms to detect differences in the intensity of use between the two. This approach allows the recognition of bimanual tasks and offers an overview of the relative use between one arm and the other, but still lacks in providing information about the functional arm use.
Additional relevant information to assess arm movement can be offered by embedded sensors, such as Inertial Measurements Units (IMUs) [29]: these devices are composed of an accelerometer, a gyroscope, and a magnetometer, and the combination of the data acquired by these three different sensors is integrated to provide information regarding the orientation of the IMU. This measure can be obtained by combining roll, pitch, and yaw angles, which are estimated from acceleration and gyroscopic data through the application of sensor fusion techniques [30]. Thanks to their compact size and the reliability of the acquired data, these sensors are a common choice to perform activity registration in natural settings.
The study conducted by Subash et al. [31] focused on the comparison between different techniques to quantify upper arm use based on data acquired through a wrist-worn IMU. In particular, the authors compared the effectiveness of Gross Movement score (GM), Thresholded Activity Counts (TAC), and machine learning methods. GM is a metric similar to the AC, with the improvement of discriminating between 'functional movement' and 'non-functional movement' relying on the information about the orientation of the IMU. The absolute change in yaw and pitch angles is analyzed, and if its value appears to be higher than 30°, coupled with an absolute elevation of the forearm with respect to the horizontal plane lower than 30°, the movement is classified as functional. The inclusion of pitch and yaw angles in the discrimination of functional and non-functional movement introduces the concept of exploration of the space in front of the subject, the 'functional space', which allows the achievement of a more comprehensive evaluation of arm motion. A hybrid metric, given by the combination of GM and TAC, has been proposed by the authors with the intent to obtain good results both for sensitivity and specificity. Lastly, the study examined three machine learning methods for the classification between functional and non-functional movements, namely Random Forest (RF), Support Vector Machine (SVM) with a radial basis function, and Multi-Layer Perceptron (MLP) algorithms. These methods were tested in both inter-subject

and intra-subject scenarios. The best results in terms of sensitivity and specificity were obtained by the machine learning techniques, and in particular, among these, RF performed slightly better (Youden index =0.74 for intra-subject measures). This study demonstrates that properly trained machine-learning methods can use IMU data to assess accurately upper arm use, outperforming traditional methods such as TAC and GM.
The research in the state of the art conducted in this thesis has revealed the prominent role of machine learning techniques in the domain of upper limb functionality monitoring. Gomez-Arrunategui et al. [32] proposed a device equipped with an IMU, which is intended to be worn on the wrist, that exploits machine learning algorithms for the recognition of functional movements and in particular of reaching actions. Since the intended application of this device is the domestic environment, reaching movements have to be recognized among the execution of complex tasks, which are typical of the ADLs, in an uncontrolled environment. To gain a comprehensive understanding of the device's versatility among various settings, the acquisition protocol included two datasets: a functional assessment dataset including tasks taken from protocols for the application of clinical scales (FMA-UE and ARAT), and an ADL dataset composed by data acquired during the preparation of a pizza and during walking. Data were acquired through a tri-axial IMU integrated into the device, namely Arm Rehabilitation Monitor (ARM), a sensor for activity counts detection, and a video camera. The ground truth, which is the sequence of labels of 'reach' and 'non-reach' associated to the movements in the dataset, was determined through video labeling. Frames were labeled as 'reach' if a sequence of forward, stationary, and backward movement was detected. The filtered and segmented data were used to train, validate and test two different classificators: RF and Convolutional Neural Network (CNN). The RF classifier was composed of 50 trees exploiting 63 signal-based features and 6 correlation features. The CNN architecture was composed by 3 convolutional layers, the learning rate was set to 0.001, and the batch size to 32. The assessment of the performance of the two algorithms was conducted with different combinations of datasets in training and testing. In the first experiment, both the training and testing sets consisted of clinical exercises. In the second experiment, exercises taken from the ADL dataset were used for both training and testing. Lastly, the third experiment aimed to assess the algorithms' ability to classify among different datasets, and thus the training set comprised standard activities while the test set included activities of daily living. The results shown that the best classification accuracies were achieved with the first experiment (92.4% for RF and 92.2% of CNN), while the worst ones were obtained with the third experiment (74.8% for RF and 76.5% of CNN). This outcome is comprehensible given that training and testing have been conducted using different datasets. While it is crucial to classify whole functional movements like reaching one, it is essential to recognize that the motion of the upper limb is far more intricate. Moreover, due to the variety of objects encountered during ADL, functional movements encompass a large variety of actions. However, each functional movement can be represented as a sequence of building blocks motions, namely primitives [33]. A more refined classification of movements can be achieved by attempting to classify functional primitives.

1.3.3 Machine learning for primitive classification

The characterization of movements during the execution of ADLs can be challenging due to the presence of an uncontrolled environment. Schambra et al. [34] proposed a taxonomy for the description of upper limb motion based on a hierarchical structure that encompasses the definition of 'activity', 'functional movement', and 'functional primitive' as depicted in Fig:1. At the top of the pyramid in Fig:1 long-duration motions are illustrated. 'Activity' is defined as a sequence of motions aimed at achieving a unique purpose through multiple small tasks, called functional movements. Functional movements, similarly to activities, can be further segmented into functional motor primitives. Motor primitives are characterized by a duration within milliseconds to seconds and are oriented at the accomplishment of one single goal. Primitives can thus be considered as the units of motion since they result in simple motion phenotypes which are consistent across activities and motor-impairment levels [34] [35]. A recent study [35] added further discrimination of the 'reach' primitive into 'reach to grasp' and 'point'. The former stipulates that the movement should end with a grasping of an object, while the latter does not involve the interaction with items.
The first study that approaches the classification of motion primitives is the one conducted by Guerra et al. [36]. Their research focused on machine-learning techniques, specifically logistic regression, applied to data streams collected from both healthy and stroke subjects using 7 IMUs positioned on the upper limb. The dataset was obtained through the acquisition of data from the execution of radial activities, which require the interaction of the patient with objects placed on a table, shelf activities, with objects distributed at different heights, and feeding activities. The definition of the ground truth was carried out with a video-labeling procedure. In particular, the authors performed the recognition of the following primitives: rest, reach-to-grasp, and release-to-retract when there was no object manipulation, and transport, manipulation, and stabilization when the action was exerted on a target object. Three subtypes were also considered including cyclic manipulation, stabilization-transport, and stabilization-manipulation. The classification performance was evaluated only for rest, reach, retract, and transport primitives. Labeled data was pre-processed, statistical descriptors were extracted using a sliding window approach, and a Hidden Markov Model (HMM) was used for pattern recognition. Finally,

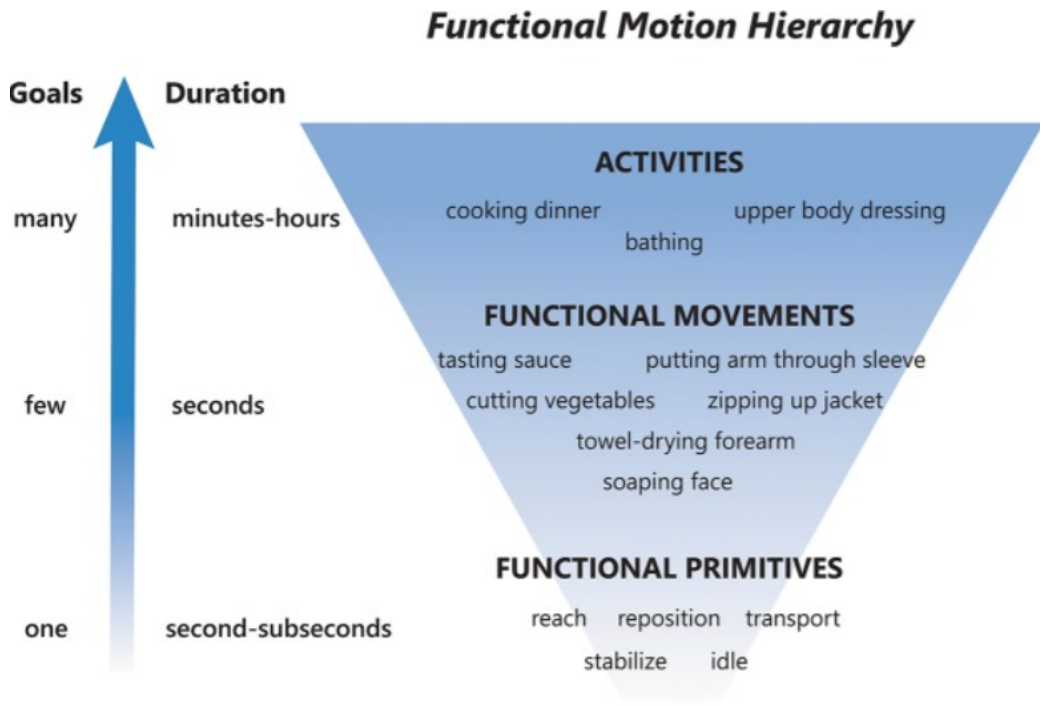

Figure 1: Image taken from Schambra et al.[34] representing the hierarchy of functional motion

a logistic regression algorithm was employed to map the predictions of functional primitives. The results demonstrated that the approach successfully identified functional movement primitives in both healthy control and stroke patients, achieving an average precision of around 80%. The authors underlined that given the good performance of IMU-based motion capture and HMM algorithm, their methodology could be applied in the quantification of rehabilitation training dose.
Another approach to primitive classification was proposed by Parnandi et al. [37]. In their paper, they outlined a pipeline to classify and count functional primitives during stroke rehabilitation exercises. This consisted in the application of a deep-learning algorithm applied to motion data to generate sequences of primitives. Kinematic information given as input to the neural network was captured with 9 IMUs. Moreover, The authors developed an algorithm that counts primitives to provide a measure of the training dose. The architecture of the deep learning algorithm was inspired by speech recognition methods and, in particular, they employed sequence-to-sequence (seq2seq) algorithms. Seq2seq are characterized by two main subsequent structures: an encoder and a decoder. The encoder elaborates the temporal sequence given as the input to generate, as the output, a single-feature vector which is then decoded by the decoder. The decoder generates as output a sequence of primitives that subsequently is then passed to an algorithm that merges subsequent similar ones and counts them. The layers of the encoder and the decoders are constituted of Gated Recurrent Units (GRU) which belong to the family of Recurrent Neural Network (RNN). These units have been specifically designed to handle long sequential data and resolve the problem of vanishing gradient which is typical of the standard RNNs. In RNN in fact, information travels through the neural network from the input neurons to the output neurons, while the error is calculated and propagated back through the network to update its weights. In these networks, a cost function is evaluated at each point by means of the comparison of the received input and the desired one and then backpropagated through the network in order to update neurons' weights. When the weights are backpropagated, they are basically multiplied neuron by neuron, and if their value is too small it will vanish over time. GRU and Long Short Term Memory (LSTM) networks have the ability to solve this problem by implementing an update and forget gate that can select the necessary information to propagate both short-term and long-term dependencies in sequences. The dataset used for the training and testing of the proposed algorithm was obtained by acquiring data from 41 chronic stroke patients performing a set of nine rehabilitation exercises taken from a standardized manual of occupational therapy. Data were acquired through 2 cameras and 9 IMUs. As in previous similar studies, the videos were labeled to populate the ground truth sequence to be associated with the kinematic data of the IMUs. The definition of primitives followed the taxonomy, previously described, proposed by Schambra et al. [34]. The movements were therefore classified among 5 primitives: idle, reach, transport, stabilize, and reposition. To assess the validity of the proposed algorithm, namely 'PrimSeq', the authors compared its performance with CNN, RF, and Action Segment Refinement

Framework (ASRF) which are three benchmark models used for activity recognition. Results demonstrate that PrimSeq outperformed the other algorithms obtaining a percentage of true counts for different primitives between 86.6%; and 99.6%. The study also shows that IMU-based motion capture can be well tolerated by patients, and the automatic primitive counts operated by PrimSeq can considerably reduce the time and effort required to manually quantify functional motion.
The remarkable results achieved with this paper have laid the foundation for setting up the work aimed at the classification of data. Taking inspiration from Panrandi et al.[37] research, one of the focuses of this thesis has been centered on the application of the advanced versions of RNN, namely Long-Short Term Memory LSTM and GRU, to not incur in the vanishing gradient problem. The classification of movement into motor primitives could be useful to generalize the evaluation of the performance of more complex skills, without the need to rely on benchmarks developed only for specific movements.

1.3.4 Thesis scope and open challenges

This thesis was developed to lay the foundation for the ultimate scope of the project, which is the exploitation of IMUs to provide input for the control system of the exosuit and assess upper limb movements. Continuous kinematic registration and subsequent UL functionality evaluation can be a highly valuable tool in home-based rehabilitation both for the patient and the practitioner. The implementation of proper data storage and transmission system could allow the specialized practitioner to receive continuous information about arm use during everyday life. This information could then be exploited to personalize the training program according to the patient's progresses. The patient, on the other side, could track his quantity and quality of arm use by means of daily reports. The reported feedback can enhance the enthusiasm of the user in the usage of wearable robots for daily assistance[9].
This research work focused on the attainment of two preliminary objectives necessary to achieve the purpose described above. The evaluation of UL motion requires, in fact, the extraction of different kinematic measures which can be easily achieved through the tri-axial IMUs embedded in the exosuit to implement a gravity compensation mechanism. These sensors can provide information regarding accelerations, angular velocities, and magnetic field strength along three orthogonal axes (x,y,z). This information can be exploited provided that their positioning in terms of orientation on the body segments is well known.
In the context of this thesis, it is planned that the positioning of the sensors will be carried out directly by users without the assistance of specialized practitioners. In light of this, the calibration procedure becomes crucial to compensate for any potential mispositioning of the sensors and ensure that the acquired data is interpretable and reliable for control and evaluation purposes. For this scope, a fast and automatic calibration procedure has been proposed.
Once the calibration is ensured, a kinematic model of the upper limb is required in order to implement a real-time control strategy for exosuit motor torques and assess movement quality. In relation to this specific scope, the mathematical extraction of 5 anatomical angles according to the definitions provided by the International Society of Biomechanics (ISB) [38] has been presented. This mathematical explanation is, in fact, lacking in the literature, given that different studies have extracted angles without following the standard (ISB) convention [39], [40] or by partially defining shoulder and elbow joints [41]. The second objective of this thesis was developed considering that the broader aim of the research is the UL movement assessment in home scenario: the data are in fact acquired in a non-controlled environment in which complex functional movements can be performed. During the execution of ADLs typically non-standardized, non-repetitive, and non-functional movements can be involved, and therefore the classification is necessary to identify the portion of data which are meaningful for the extraction of evaluation metrics. For this reason, the application of a deep-learning algorithm for fine-grained classification of motion was implemented. The idea is that the classification can provide meaningful information which can ultimately be used to select which data are significant for the evaluation of motion metrics. The idea was to attempt the classification of motion primitives using advanced RNN architectures, similar to what was proposed by Parnandi et al. [37]. In contrast to their study, which involved the exclusive use of data acquired from standard settings, the acquisition protocol proposed in this thesis included both standard and non-standard activities. This choice arises considering that the final application of the exosuit will be in an uncontrolled environment. Moreover, this research distinguishes from previous studies [36], [37] for the number of sensors involved. The data supplied to the deep learning algorithm were obtained through the acquisition of only 3 IMUs: this choice was constrained by the design characteristics of the exosuit. For what concerns the selection of data to provide to the network, only ISB angles, extracted with the approach proposed in the context of this thesis, and the relative accelerations and angular velocities between segments have been chosen. The selection of such few features (26), compared for instance with the 77 identified by Panrandi et al., was driven by the intention to preserve data interpretability and contemporarily reduce the computational effort of the algorithm.

2. Materials and methods

The following section describes the materials and methods employed to achieve the objectives of the thesis. First, the procedure defined to compute shoulder and elbow upper limb joint angles from IMUs data will be described followed by the validation experiments. Then, a description of the experiments to acquire the dataset used for the classification network training will be provided, followed by a description of the network itself.

2.1. IMU-based estimation of upper-limb angles

This section unfolds a method for calibrating the IMUs when worn by the users and extracting shoulder and elbow anatomical angles starting from the rotation matrices following the ISB convention [38].

2.1.1 Materials

The IMU sensors employed in this project are the NGIMUs (x-io Technologies Limited Bristol, UK), shown in Figure 2. NGIMUs embed different sensors among which there are a tri-axial accelerometer for the measure of linear acceleration, a tri-axial gyroscope for the measure of angular velocity, and a tri-axial magnetometer that exploits the Hall effect to detect the intensity of the magnetic field. NGIMUs are equipped with other transducers (humidity, temperature, and pressure sensors) which will not be used in the current application. NGIMUs employ sensor fusion combining data from accelerometers, gyroscopes, and magnetometers to provide an accurate measure of the orientation of the device. This estimation is performed through the application of the Madgwik algorithm [30] which iteratively updates the orientation estimation, providing an accurate representation of the object's orientation in real-time.
NGIMU's proprietary software allows the synchronization of multiple sensors and their communication via a wireless protocol which requires the use of a router. Moreover, these sensors are equipped with a battery that allows a cable-free application. The software provided by the owning company is open source, and Python sample codes to establish the communication between NGIMUs and computers are provided on the GitHub official page of the company.
In the context of this project, in which the intended application is at-home use, magnetometers had to be switched off to ensure data accuracy and minimize the introduction of errors caused by magnetic interference typical of an indoor environment. This requirement carries out two main drawbacks. The first is the necessity to align the sensors on a rigid surface in order to reset their yaw angle and ensure that they share the same ground reference frame, the second is the appearance over time of a drift in the measure of the orientation, in particular of the yaw angle, introduced by the lack of compensation that is usually implemented through magnetometer data. For validation purposes, TIAGo robot (PAL Robotics Barcelona, Spain) and BTS SMART DX 400 (BTS SPA, Italy) were used. In Figure 3 TIAGo robot (A) and a schema of an optoelectronic system (B) are represented.

Figure 2: NGIMU sensors (x-io Technologies Limited Bristol UK, USB station for simultaneous charging of multiple IMUs and TP-link router (TP-Link Corporation Limited) for wireless connection

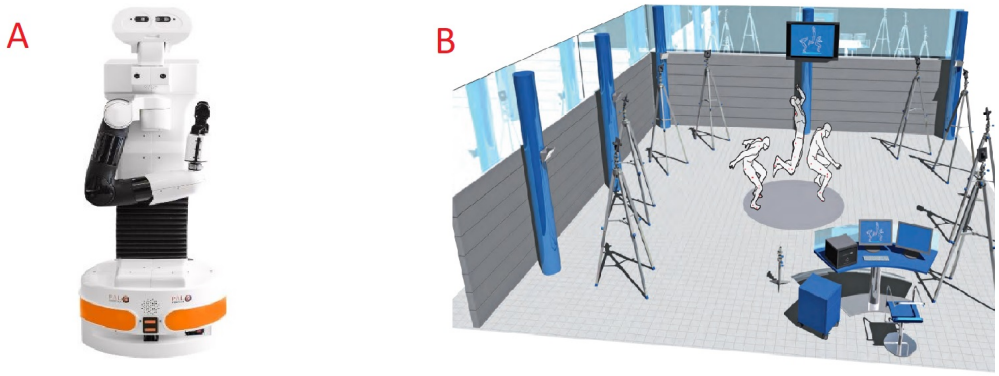

Figure 3: A) TIAGo robot, B) BTS SMART DX 400 Optoelectronic system

More in detail, TIAGo is a humanoid robot, mainly used for research purposes, equipped with motors, that provide 7 Degrees Of Freedom (DOFs), and encoders for an accurate joint reading [42]. The encoders' data were used as the ground truth for robot joint angle comparison. The optoelectronic system, located at 'Luigi Divieti' laboratory at Politecnico di Milano, is instead equipped with 8 high-frequency video cameras (100fps) and a proprietary software for calibration and marker trajectories extraction and visualization. The angles extracted by the optoelectronic system were used as ground truth for human joint angle comparison.

2.1.2 Reference frames definition

The reference frames that will be used in the following sections are defined as shown in Figure 4 and are:

- Global reference frame (G), defined with the z-axis pointing vertically up, and the x-axis and y-axis oriented as to obtain an orthogonal frame.
- IMU reference frame (I), that can be oriented randomly on the limb.
- Body segment reference frame (B), fixed to each body segment and defined with the z-axis parallel to the segment pointing up, the y-axis pointing forward, and the x-axis pointing to the right.
- ISB convention reference frame (ISB), fixed to each body segment and defined with the y-axis parallel to the segment pointing up, the x-axis pointing forward, and the z-axis pointing to the right.

When left joints are concerned, the same reference frame was used and, when needed, a term was applied that is defined as:

$$\kappa = \begin{cases} +1, & \text{if right arm} \\ -1, & \text{if left arm} \end{cases} \tag{1}$$

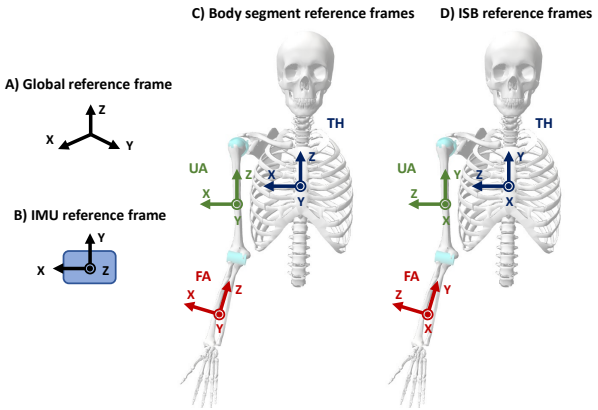

Figure 4: A) Global, B) IMU, C) Body segment, D) ISB reference frames. TH indicates the thorax, UA indicates the upper arm, FA indicates the forearm.

2.1.3 Calibration procedure

The calibration procedure is needed to align the IMUs reference frames (I) and the body segments reference frames (B). Calibration is performed by acquiring data from two different poses: i) the N-pose (A in Figure 5) and ii) the T-pose (B in Figure 5). During the N-pose, the user stands still with the arms resting and the palms of the hands pointing forward. In this configuration, the ISB joint angles are ideally null.
The orientation of each IMU with respect to G is expressed by the rotation matrix estimated by the IMU and can be expressed as:

$$R_{I_i}^{G} = R_{I_i,0}^{G} R_{I_i}^{I_i,0} \tag{2}$$

where $R_{I_i,0}^{G}$ is the rotation matrix of the i-th IMU during the N-pose, and $R_{I_i}^{I_i,0}$ is the rotation matrix of the i-th IMU calibrated with respect to the N-pose. Inverting Eq. (2), the following equation was obtained:

$$R_{I_i}^{I_i,0} = (R_{I_i,0}^{G})^T R_{I_i}^{G} \tag{3}$$

The orientation of each IMU with respect to G is also expressed as:

$$R_{I_i}^{G} = R_{B_i}^{G} R_{I_i}^{B_i} \tag{4}$$

where $R_{B_i}^{G}$ is the rotation matrix describing the orientation of the i-th body segment with respect to G, and $R_{I_i}^{B_i}$ is the rotation matrix describing the orientation of the i-th IMU with respect to the i-th body segment. This rotation matrix is assumed to be constant during the subsequent use of the sensors, such that $R_{I_i}^{B_i} = R_{I_i,0}^{B_i,0}$,where 0 indicates the N-pose configuration. If the sensors are moved relative to the body segments, the calibration procedure should be performed again.
The rotation matrix describing the orientation of the body segment with respect to G can be expressed as:

$$R_{B_i}^{G} = R_{B_i,0}^{G} R_{B_i}^{B_i,0} \tag{5}$$

where $R_{B_i,0}^{G}$ is the rotation matrix of the i-th body segment with respect to G in the N-pose and is unknown, and $R_{B_i}^{B_i,0}$ is the rotation matrix describing the orientation of i-th body segment at the current time instant with respect to the N-pose.
Using Eq. (5), Eq. (4) can be rewritten as:

$$R_{I_i}^{G} = R_{B_i,0}^{G} R_{B_i}^{B_i,0} R_{I_i}^{B_i} \tag{6}$$

During the T-pose, the arms are rotated by 90° in the coronal plane. In this configuration, the ISB joint angles are ideally null except for AOE which is equal to 90°.
Assuming that in the N-pose the z-axes of the body segments are aligned with the z-axes of the IMUs calibrated as in Eq. (3) and the z-axis of G, the rotation matrices expressing the orientation of the body segments with respect to G in the N-pose can be expressed as a rotation around the z-axis of an angle θ:

$$R_{B_i,0}^{G} = R_z(\theta) \tag{7}$$

$$\theta = \angle(X_G, -\kappa Z_{I,calib_{UA}}) \tag{8}$$

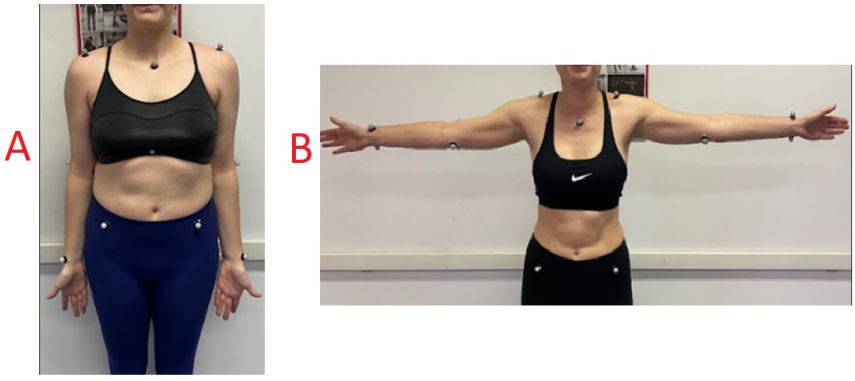

Figure 5: A) N-pose B) Tpose

where X_G is the x-axis of G (namely $[1,0,0]$), and $Z_{I,calib_{UA}}$ is the z-axis of the IMU placed on the upper arm and calibrated with respect to the N-pose. If the user can't reach an AOE angle of 90°, θ can be estimated with the negative of the projection of the z-axis of B on the horizontal plane (G x-y). Eq. (4) can be rewritten for the N-pose as:

$$R^G_{I_i,0} = R_z(\theta)R^{B_i}_{I_i} \tag{9}$$

The expression of $R^{B_i}_{I_i}$ is then obtained reversing Eq. (9):

$$R^{B_i}_{I_i} = R_z(\theta)^T R^G_{I_i,0} \tag{10}$$

Substituting Eq. (7) and Eq. (10) in Eq. (6) it results:

$$R^G_{I_i} = R_z(\theta)R^{B_i,0}_{B_i}(R_z(\theta)^T R^G_{I_i,0}) \tag{11}$$

Finally, inverting Eq. (11) the following expression is obtained:

$$R^{B_i,0}_{B_i} = R_z(\theta)^T R^G_{I_i}(R_z(\theta)^T R^G_{I_i,0})^T \tag{12}$$

where $R^G_{I_i}$ is the rotation matrix estimated from the i-th IMU, and $R^{B_i,0}_{B_i}$ is the matrix that represents, for the i-th body segment, its orientation in space calibrated with respect to the N-pose and expressed in body coordinates. Once this matrix is obtained for each body segment, it must be rotated to be expressed in the ISB reference frame:

$$R^{ISB_i,0}_{ISB_i} = R^{B_i,0}_{B_i} R_x\left(\frac{\pi}{2}\right) R_y\left(\frac{\pi}{2}\right) \tag{13}$$

This expression is valid both for the right and the left arm.

2.1.4 ISB upper limb angles definition

Shoulder and elbow anatomical angles are defined by the International Society of Biomechanics (ISB) [38], in which joints coordinate systems for the shoulder, elbow, wrist, and hand are described. Given that the analysis of wrist and hand motion is outside of the scope of this thesis, only shoulder and elbow joint coordinate systems will be presented.
The shoulder orientation convention is defined as the rotation of the humerus relative to the thorax following a Y-X-Y (according to the ISB reference system) sequence of Euler angle rotations. The first rotation around the Y axis defines the Plane Of Elevation angle (POE)(positive when moving the arm frontally), the rotation around X the Angle Of Elevation (AOE) (positive when elevating), and the last rotation around the Y axis represents the Humeral Rotation (HR)(positive when the rotation is internal).
The elbow joint is defined as the motion of the forearm relative to the humerus as a Z–X–Y rotation sequence. The first rotation around Z is addressed as Flexion-Extension (FE) angle and the rotation around Y as the Pronation-Supination angle (PS),. The rotation around X, which is descriptive of the ulnar deviation, will not be taken into account for this study and considered negligible.
The rotation matrix describing the orientation of the upper arm body segment (ISB,UA) with respect to G can be defined as:

$$R^G_{ISB,UA} = R^G_{ISB,TH} R_y(\kappa POE) R_x(-\kappa AOE) R_y(\kappa HR) \tag{14}$$

where $R^G_{ISB,TH}$ is the rotation matrix of the thorax body segment with respect to G. R_x, R_y represent the rotation matrices deriving from the rotation respectively around the x and y-axis of the angles indicated between parenthesis. The rotation matrix describing the orientation of the forearm body segment with respect to G can be defined as:

$$R^G_{ISB,FA} = R^G_{ISB,UA} R_z(FE) R_y(\kappa PS) \tag{15}$$

2.1.5 ISB angle computation

For the sake of clarity, $R^{ISB_i,0}_{ISB_i}$ will be referred for each body segment as TH for the thorax, UA for the upper arm, and FA for the forearm.
The POE can be computed as:

$$POE = \angle(proj_{XZ_{TH}}(Y_{UA}), -\kappa Z_{TH}) \tag{16}$$

that is the relative angle between the projection of the y-axis of UA (Y_{UA}) onto the plane defined by the x-axis and the z-axis of TH (XZ_{TH}), and the z-axis of TH. It is worth remarking that, in the particular case of a null AOE Y_{UA} is orthogonal to XZ_{TH}, thus the projection $proj_{XZ_{TH}}(Y_{UA}$ degenerates to a point, and Eq. (16)

loses its significance. This means that the POE is ill-defined when AOE is null. Indeed, if AOE is null, POE and HR coincide.
The AOE can be computed as:

$$AOE = \angle(Y_{UA}, Y_{TH}) \tag{17}$$

that is the relative angle between the y-axis of TH and the y-axis of UA.
Inverting Eq. (14), HR can be computed as:

$$R_y(HR) = (R_x(-\kappa AOE))^T (R_y(POE))^T (TH)^T UA \tag{18}$$

$$HR = tan^{-1}([R_y(HR)]_{1,3}, [R_y(HR)]_{1,1}) \tag{19}$$

where $[A]_{i,j}$ indicates the element of the matrix at the i-th row and j-th column.
FE can be computed as:

$$FE = \angle(Y_{FA}, Y_{UA}) \tag{20}$$

that is the relative angle between the y-axis of UA and the y-axis of FA.
Inverting Eq. (15), PS can be computed as:

$$R_y(PS) = (R_z(FE))^T (UA)^T FA \tag{21}$$

$$PS = tan^{-1}([R_y(PS)]_{1,3}, [Ry(PS)]_{1,1}) \tag{22}$$

Preliminary tests on subjects have shown that when the AOE has small values, the estimation of HR and POE is biased due to the fact that, in this specific case, $proj_{XZ_{TH}}(Y_{UA}$ may not be accurate. In this particular case, the discrimination between POE and HR is challenging. Moreover, the soft tissues between the humerus and the IMU can corrupt the estimation of this angle due to the presence of a relative movement between the sensor and the bone. For these reasons, inspired by Rab and colleagues [43], an alternative method for the estimation of HR which reconstructs UArotation matrix exploiting the orientation on the flexed FA is proposed.
Assuming a null ulnar deviation and given the definition of the relationship between FA and UA rotation matrices (15), the movement of the forearm should always occur in the plane composed by the x-axis and y-axis of UAXY_{UA}. By exploiting this property, it is possible to define an alternative UA rotation matrix UA_{corr} which takes into account the position of FA when it is flexed. The direction of the x-axis of UA_{corr}, namely $Y_{UA_{corr}}$, was defined to be equal to the one of the normalized projection of Y_{FA} onto the plane defined by x-axis and z-axis of UA(XZ_{UA}):

$$projY_{FAUA} = |Y_{UA} Y_{FA}| \tag{23}$$

$$v = (projY_{FAUA} Y_{UA}) - Y_{FA} \tag{24}$$

$$X_{UA_{corr}} = v/|v| \tag{25}$$

$projY_{FAUA}$ represents the projection of the y-axis of FA onto the y-axis of UA. Given that the y-axis of the upper arm is well defined independently on the AOE or FE, $Y_{UA_{corr}}$ has been defined to be equal to Y_{UA}. $Z_{UA_{corr}}$ is defined considering that $X_{UA_{corr}}$, $Y_{UA_{corr}}$ and $Z_{UA_{corr}}$ should define an orthogonal basis.

$$Z_{UA_{corr}} = X_{UA_{corr}} \times Y_{UA_{corr}} \tag{26}$$

Finally, the variant of the HR , namely HR_{corr}, can be computed exactly like in 14:

$$R_y(HR_{corr}) = (R_x(-\kappa AOE))^T (R_y(POE))^T (TH)^T UA_{corr} \tag{27}$$

$$HR_{corr} = tan^{-1}([R_y(HR_{corr})]_{1,3}, [R_y(HR_{corr})]_{1,1}) \tag{28}$$

The same "corrected" UA rotation matrix was used to estimate an alternative PS angle, namely PS_corr:

$$R_y(PS) = (R_z(FE))^T (UA_corr)^T FA \tag{29}$$

$$PS_corr = tan^{-1}([R_y(PS_corr)]_{1,3}, [Ry(PS_corr)]_{1,1}) \tag{30}$$

These two additional corrected angles were exploited only in the validation of healthy participants since the need for their computation became apparent after moving from the robotic arm to the human arm.

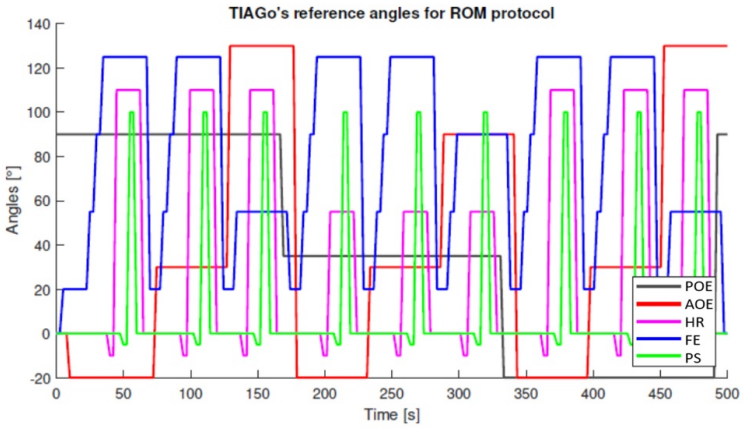

Figure 6: TIAGO's joint trajectories during validation protocol. *POE* is shown in black, *AOE* in red, *HR* in pink, *FE* in blue, and *PS* in green. The image was taken from the thesis work of Bortlein C.

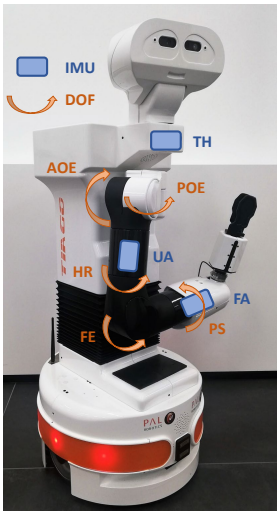

Figure 7: TIAGo robot and a drawing showing the IMU positioning (in blue) and the relevant angles (in orange). Image taken from [44].

2.2. Experimental validation

The validation of the proposed calibration and anatomical angle extraction method has been conducted in two phases. The first phase consisted in the comparison of the data obtained with the proposed procedure and those acquired by means of TIAGo's encoders. During the second phase, the validation on participants has been performed by comparing the angles obtained with the proposed approach to the ones extracted with the optoelectronic system described in section 2.1.1.

2.2.1 Validation on the robotic arm

The first phase of the experimental validation was conducted by comparing the values of the ISB angles estimated from the IMUs with the angles measured by the encoders of the TIAGo robot during the execution of a set of movements. The movements were designed to explore as many angle combinations as possible within the human range of motion. The trajectories of the TIAGo joints during the execution of validation tests are depicted in Figure 6. They are composed of sets of *FE*, *HR* , and *PS* trajectories repeated for varying values of *AOE* and *POE*. The IMUs were positioned on TIAGo's head, which moves in solidary with the thorax, arm, and forearm as shown in Figure 12.
The experimental protocol for validation consisted in the execution of tests starting with the registration of TH, UA, and FA rotation matrices while TIAGo's arm was set in N-pose and T-pose configurations. These data were used to perform the calibration procedure described in section 2.1.3. Since TIAGo N-pose cannot be set via software control, its arm was manually fully extended and aligned vertically.

Joint	Bony landmark
Neck (2 markers)	7th cervical vertebrae Sternum jugular notch
Right hip	Anterior superior iliac spine
Left hip	Anterior superior iliac spine
Sacrum	Sacrum
Right shoulder	Acromion
Left shoulder	Acromion
Right elbow (3 markers)	Lateral epicondyle of humerus Medial epicondyle of humerus olecranon
Left elbow (3 markers)	Lateral epicondyle of humerus Medial epicondyle of humerus olecranon
Right wrist (2 markers)	Radius-Styloid process Ulna-Styloid process
Left wrist (2 markers)	Radius-Styloid process Ulna-Styloid process

Table 1: List of markers' location and relative bony landmarks.

Two tests were conducted namely, 'Test 1' and 'Test 2'. During Test 1, the IMUs were positioned aligning the y-axis of the sensors with the robot's segments. Test 2 was instead conducted after positioning the IMUs in a non-aligned way in order to test the reliability of the proposed calibration and angle extraction methods in the event of the occurrence of mispositioning.
Data acquired from TIAGo encoders (35Hz) and IMUs (150Hz) were synchronized by timestamps comparison. Finally, the root mean square error (RMSE) and the correlation coefficient (r) were computed for each test and each ISB angle. The proposed method for ISB angle computation and the results of the validation against TIAGo were published in VIII Congress of the National Group of Bioengineering (GNB) [44].

2.2.2 Validation on healthy participants

A second validation was conducted on healthy subjects by means of an optoelectronic system. 5 subjects (mean age=24, 2 male, 3 female, 4 right-handed, 1 left-handed) were included in the acquisition protocol and provided their informed consent for their participation in research projects in accordance with the guidelines established by the Politecnico di Milano . 17 reflective markers were positioned on bony landmarks of the thorax, upper arm, and forearm as suggested in Rab et al. [43]. Table 1 provides an indication of markers' positions and the respective bony landmarks.
5 IMUs were positioned on the thorax, right and left upper arms, and right and left forearms as depicted in Figure 8.
Differently from what was done for the validation on the robotic arm, the acquisition protocol consisted of 5 simple tasks, aimed at exploring one single joint at time. Specifically, the tasks were defined as follows:

- Task 1: *POE* exploration. Subject seated with AOE=90°, FE=0° and PS=180°. Arm was moved from left to right and vice versa exploring the whole range of motion of the POE. ;
- Task 2: *AOE* exploration. Subject seated with FE=0° and PS=180°. Arm was moved up and down and vice versa ;
- Task 3: *HR* exploration. Subject seated with FE=90°, AOE=90°, and PS=180°. The humerus was rotated internally and externally;
- Task 4: *FE* exploration. Subject seated with FE=90°, AOE=90°, and PS=0°. The elbow was flexed and extended ;
- Task 5: *PS* exploration. Subject seated with FE=90° and AOE=0°. The wrist was rotated internally and externally ;

Each task was repeated 3 times for each arm. For tasks 2, 3, 4, 5 for each repetition, the *POE* was changed. Drift control was performed after completing each task by checking the *POE* values during the T-pose and the *PS* values with null joint angles except for a *FE* of 90°. If a drift was observable, usually 5°-10°, the calibration procedure and the task after which the drift was detected were repeated. In order to reset the drift and re-perform the calibration, the IMUs had to be detached from the subject, aligned on a rigid surface, and

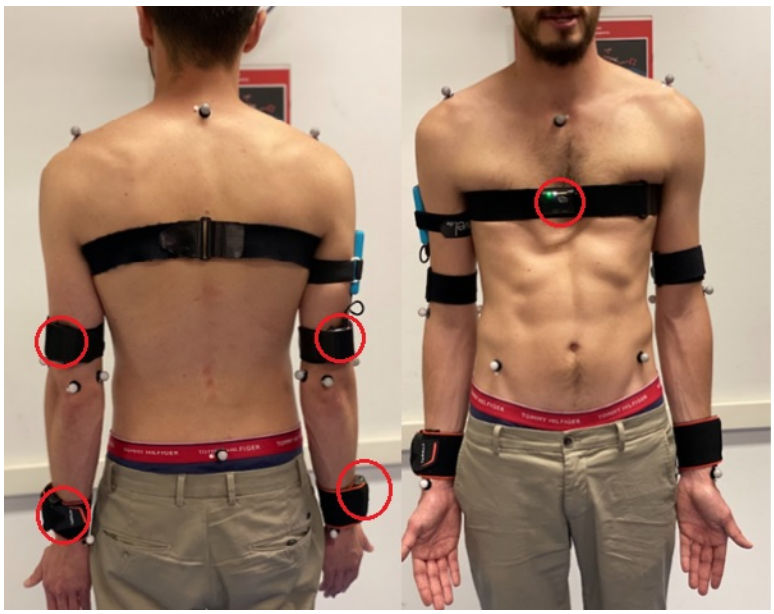

Figure 8: Markers and IMU positioning on one participant. The IMUs are indicated with a red circle. The white/gray dots are markers.

re-initialized by sending a reset command with the NGIMU proprietary software.
IMU data were acquired at 50Hz, while videos of the optoelectronic system were recorded at 100fps. The extraction of ISB angles with the optoelectronic system was automatically performed by BTS proprietary software in which, YXY and ZXY conventions were set respectively for the shoulder and elbow joint definition. To enable a comparison between the two measurement systems data were processed in Matlab (Mathworks Inc. Natick, Massachusetts) environment. Signals acquired with the IMUs were oversampled to 100Hz in order to match the sampling frequency of the optoelectronic system. Subsequently, a data integrity assessment was conducted, followed by the removal of portions of data that were undefined and presented as 'NaN'. When necessary, signals' discontinuities were eliminated. This was needed since, given the way angles are computed, they 'wrap' their values when exceding a certain threshold. For example, in the condition in which an angle overcomes 180°, its next computed value would be -180°.
Given the ultimate goal of evaluating the correlation between corresponding signals between optoelectronic and IMU measures, a point-wise subtraction between each sample in a repetition and the mean of all samples contained in that repetition was performed. This approach was necessary because signals often exhibited an offset between optoelectronic and IMU measures. Morover, for assessment purposes, is indeed more relevant to observe the ROM rather than the absolute angles. Zero-mean signals were then aligned in time by means of the cross-correlation among them: one signal was shifted in time by a value equal to the lag corresponding to the maximum value of cross-correlation between signals. The portions of the signal that did not overlap were then trimmed. Finally, the RMSE, RMSE%, and correlation coefficients (r) were extracted to perform the comparison between IMU-based and optoelectronic measurements. The corresponding Bland-Altman plots were also drawn. In particular, for tasks 1, 2, 3, 4, and 5 these metrics were extracted only for the angle of interest.

2.3. Classification of motor primitives

To enable the classification of primitives in both simple ADL (SADL) and complex ADL (CADL) movements, a data acquisition protocol was designed. This protocol facilitated the systematic collection of data, which was subsequently used for training, validating, and testing the deep learning algorithm.

2.3.1 Experimental setup

10 volunteers (1 male, 9 females, mean age=30.5, 3 left-handed, 7 right-handed) participated in the data acquisition process. The inclusion criteria consisted of 18 years of age, good overall health, and no presence of upper limb impairments. Prior to data acquisition, the subjects provided their informed consent in accordance with the guidelines established by the Politecnico di Milano for their participation in research projects. The experiments were approved by the ethical committee of Politecnico di Milano. The acquisitions were carried

out at the WECOBOT laboratory (Lecco campus, Politecnico di Milano).
Kinematic data were recorded with 5 NGIMU sensors attached on body segments with Velcro straps. They were positioned on the thorax, right and left upper arm, and right and left forearm. In order to capture even small variations in upper arms and forearms configurations, the sensors were positioned on the lower part of the segments, as shown in Figure 8. A GoPro HERO 5 (GoPro Inc.) set at 24fps was used for video acquisition. Communication with IMUs was possible through a custom-made Python script which also enabled data storage into .csv files. At the beginning and at the end of each exercise, a command was sent to all the IMUs in order to make them blink. The time of appearance of the led blinking was supposed to be the initial time at which data were saved in the .csv file. This feature was in fact employed to perform an initial synchronization of videos and IMU data. A Python GUI was implemented to support and facilitate the acquisition process.

2.3.2 Acquisition protocol

The acquisition protocol consisted in the execution of two sets of activities: one including 8 simple activities (SADLs), and another one comprising the execution of 3 complex activities typical of everyday life (CADLs). Each activity in the two datasets was repeated twice for each subject, one with the right arm and one with the left arm. In the case of the CADL, the subject was asked to perform the activities two times: one as usual, and the other one paying attention in using mostly the non-dominant arm. The occurrence of drift was checked between two exercises by means of a T-pose and N-pose with 90° *FE* to assess respectively for *POE* and *PS* reliability. If a drift of more than 5°-10° was observed, the IMUs were detached from the subject, aligned, and reset to restore a shared ground reference frame. The sensors were then repositioned on the body segments, and the calibration procedure was repeated. The data acquisition process lasted on average 1:45h per subject (including explanation and sensors positioning). The set of activities defined for this thesis will be explained in detail in the upcoming sections.

2.3.3 SADL dataset acquisition

SADL activities included both seating and standing tasks. During the seating tasks, the subject was seated on a chair in front of a desk, with the possibility to move their back. Six regions were drawn on the desk and corresponded to specific positions that the subject needed to reach during the execution of different exercises. Regions 1,2,3 (R1, R2, R3) were closer to the subject while 4,5,6 (R4, R5, R6) were farther and required an elbow extension and, eventually, thorax flexion to be reached. A board with 6 regions (B1, B2, B3, B4, B5, B6), similar to the one drawn on the desk, was placed in front of the subject. The rest position corresponded to the subject with the elbow on the table and hand in region 2. The setup is displayed in Figure 9.
The items required for the execution of the sitting tasks were: a smartphone, a glass bottle, a bowl, a glass, and a spoon.
The subjects were guided vocally in the execution of different activities defined as follows:

- BOTTLE: a bottle was placed in Rn starting from R1. The subject was asked to reach and grasp the bottle in position Rn, move it to region Rn+1, leave it, and move back to the rest position. The task was repeated until reaching R6;
- POUR: a bottle of water was placed in Rn starting from R1, and a glass was always in R2. The subject was asked to reach and grasp the bottle, pour water into the glass, transport the bottle to Rn+1, and turn back to the rest position. The task was repeated until reaching R6;
- DRINK: A glass full of water was placed in Rn starting from R1. The subject was asked to reach and grasp the glass, drink water, transport the glass to region Rn+1 and turn back to the rest position. The task was repeated until reaching R6;
- PHONE: a smartphone was positioned in Rn starting from R1. The subject was asked to reach and grasp the phone, keep it close to the ear for a couple of seconds, transport it to the Rn+1, and move back to the rest position. The task was repeated until reaching R6;
- MIX: a bowl was positioned in Rn starting from R1, and a spoon was placed within R2. The subject was asked to reach and transport the bowl using both arms from Rn to R2, then to take the spoon and simulate mixing movement for a couple of seconds. The bowl was then bi-manually transported to Rn+1 and the arm moved back to the rest position. The task was repeated until reaching R6;

During the execution of the standing SADL-set, the subject stood in front of 3 shelves of different heights. Three regions were drawn on each shelf and all the regions were identified from 1 to 9 (S1-S9) as in Figure 10. In this setting, the rest position corresponded to the subject standing with arms along the sides. The items required for the execution of standing SADL tasks were: a glass bottle, a book, and 9 glass jars. The subjects were guided vocally in the execution of different activities defined as follows:

Figure 9: This figure represents the setup for seated SADL. Regions R1-R6 are represented by orange circles, while B1-B1 by blue ones

- BOOK: a book was initially placed in Sn starting from S1, the subject reached and grasped the book, simulated reading for a couple of seconds, transported the book to the region Sn+1 and turned back to rest position. The task was repeated until reaching S9;
- PLANT: 9 jars were positioned in different regions on the shelves. The subject held a bottle full of water for the entire execution of the activity and was asked to pour water into each jar starting from S1, going to S9, and moving back to the rest position every time.

2.3.4 CADL dataset acquisition

For the acquisition of the CADL-set, the protocol included three complex activities inspired by ADLs. The scope of this choice is to enrich the dataset with movements acquired in a semi-uncontrolled environment. In fact, during the execution of these activities, subjects were free to move in space and decide autonomously the sequence of action to accomplish the main goal of each exercise. The items provided to the participants were: a coffee machine, sugar bags, a spoon, a coffee cup, a closet, a trash bin, coffee pods, tea bags, cutlery, a bottle of water, bread, jam/spreadable cream, a kettle, teacup, clothes (of different sizes), clothes hangers, toothpaste, a toothbrush, soap, a towel, hair-brush, and an umbrella.
The subjects were guided vocally in the execution of different activities defined as follows:

- BREAKFAST: this macro-activity included preparing and having breakfast;
- PERSONAL CARE: typical morning bathroom activities were included such as brushing teeth, brushing hair, washing face, and washing hands. The activities involving water were simulated.
- LAUNDRY: folding and hanging clothes.

2.3.5 Ground truth identification

Before the video labeling process, each video was cut so that the first frame corresponded to the moment the IMUs started blinking following the command of 'Start exercise' sent through the GUI.
Video labeling was carried out using a custom-made Python script, allowing one to visualize a video, change the speed of frame sliding, and rewind previous frames. Most importantly this application enabled to receive keyboard inputs associated with 6 possible labels: 'idle', 'stabilize', 'reach', 'transport', 'reposition', and 'cut'

Figure 10: This figure represents the setup for standing SADL. Regions S1-S9 are represented in the figure as green circles.

(to be used when the movement was not identifiable as a primitive). These inputs were then associated with the timestamp corresponding to the frame that was displayed the moment the key was pressed. Motor primitive recognition was performed according to the following definitions:

- Reach: the purpose is to make contact with a target object. Motion is evident.
- Reposition: the purpose is to move into proximity or move away from a target object. Motion is present. There is no object contact.
- Transport: the purpose is to transport a target object in space. Motion is evident.
- Stabilize: the purpose is to hold a target object still. The motion is minimal.
- Idle: the purpose is to stand at the ready near of a target object, motion is minimal. The definition of idle was extended also to the rest position.

Video labeling resulted in the generation of a ".csv" file with timestamps and labels associated with each frame. A first synchronization between labels and IMU data was performed by means of an alignment of corresponding timestamps. However, by visually inspecting synchronized data, it was clear that in some cases there was a delay between IMU data and labels. To account for this problem, a realignment was implemented by shifting the two signals according to the minimization of the standard deviation of UL angles during 'idle' and 'stabilize' movements. Data that appeared inaccurate in terms of labeling even after synchronization were discarded.

2.3.6 Primitive classification: features and model architecture

The model used for the classification of sequences of movement into motor primitives was based on the advanced version of RNN: LSTM.
The deep learning network was built using the "Sequential" class, provided by "Keras" framework, which allowed the generation of the neural network model as a stack of sequential layers. The model included a first masking layer to assure that the algorithm ignored the null values added during zero-padding. The input shape was equal to (6, 26) where 6 is the number of samples per window, and 26 is the number of features. Then, an LSTM and a dropout layer with a dropout rate of 0.5 were added. The dropout technique was implemented to prevent overfitting given the limited dimensionality of the dataset: in fact, this layer randomly sets a fraction of input neurons to zero. Finally, a 'Dense' layer was stacked at the end of the model: this layer mapped the input of the previous layer into a number of outputs equal to one of the possible labels by means of a 'softmax' activation function. The model was compiled using Adam optimizer and categorical cross-entropy as loss function. A schematic of the model is represented in Figure 11.

Figure 11: Schema of the sequential model built for primitive classification. The number in the arrows represents the dimensionality of the input/output vector for each layer. The ML model consists of four key components: a masking layer, a LSTM layer, a dropout layer, and a dense one.

The learning rate was initially set to 0.005 as in Parnandi et al. [37] but this value led to overfitting. Its value was finally set to 0.01, according to the highest accuracy achieved following a trial and error procedure. The number of epochs was 100, which represented approximately the number of iterations at which the training accuracy stopped increasing.
The data resulting from the experimental acquisition and video labeling was a set of files containing information about coefficients of rotation matrices of the UL body segments, their linear accelerations, angular rotations along the x-axis, y-axis, and z-axis, and the 7 ISB angles defined previously. An additional angle, the one between the y-axes of TO and FA was computed. Even though this angle does not have an anatomical meaning, since it is the angle between two non-connected joints, it provides additional information that could be useful for the classification algorithm. Indeed, it is not affected by potential inaccuracies of UA angles estimation or drift.
The relative acceleration between the thorax and upper arm, thorax and forearm, and upper arm and forearm were determined by subtraction among the different segments:

$$a_{\vec{UA/TH}} = a_{\vec{TH}} - a_{\vec{UA}}; \qquad a_{\vec{FA/TH}} = a_{\vec{TH}} - a_{\vec{FA}}; \qquad a_{\vec{FA/UA}} = a_{\vec{FA}} - a_{\vec{UA}} \tag{31}$$

The same procedure was applied for the angular velocities:

$$w_{\vec{UA/TH}} = w_{\vec{TH}} - w_{\vec{UA}}; \qquad w_{\vec{FA/TH}} = w_{\vec{TH}} - w_{\vec{FA}}; \qquad w_{\vec{FA/UA}} = w_{\vec{FA}} - w_{\vec{UA}} \tag{32}$$

Each relative vector was described by 3 columns that represent the components along the three axes. The features that were given as input to the neural network were:

- 7 ISB angles: *POE AOE HR* , *FE*, *PS* , HR_{corr} , and PS_{corr}
- 3 relative linear accelerations: $a_{\vec{UA/TH}}$,$a_{\vec{FA/TH}}$, $a_{\vec{FA/UA}}$
- 3 relative angular rotations: $w_{\vec{UA/TH}}$,$w_{\vec{FA/TH}}$, $w_{\vec{FA/UA}}$
- The relative angle between y-axes of TO and FA

Prior to feeding data to the neural network, labeled IMU data was segmented in overlapping (overlap=80%) windows of size 0.12s. This value was chosen given that 6 was the length, in terms of samples (acquired at 50Hz), of the shortest primitive. The choice of the window length was consistent with the definition of minimal motion given by Schambra et al [34] which defines it as a lack of changes in upper extremity configuration for at least 0.05s.
Each windowed exercise was then split into 2 segments of dimension 80% and 20% of the total length that were saved respectively into training and testing datasets. For each exercise in the training dataset, a zero-padding function was applied to ensure that each exercise had the same size, set to be equal to that of the longest exercise. In order to allow the neural network to process a whole exercise in a single iteration, the batch size was chosen to be equal to the maximum exercise length. During training, 5% of the training dataset was used for validation purposes.

2.4. Algorithm performance assessment

To assess the performance of the algorithm, the LSTM performance was tested for different values of hidden units: in particular, 50, 100, 200, and 300 were chosen as depth values to be tested. 2 different tests were then conducted for each hyperparameter choice:

- Train and test with Dataset A: consisting in training and testing with only SADL activities.
- Train and test with Dataset B: consisting in training and testing with both SADL and CADL activities.

A total of 5 repetitions were performed for each test, in each of which the order of exercises within the dataset was randomly shuffled to ensure different sets of exercises for training and validation in each repetition. Absolute and relative f1-scores were averaged across repetitions.

3. Results and discussion

This chapter presents the results achieved in this thesis and their discussion. In the first part, the outcomes concerning ISB angle estimation are presented and discussed both for the validation with the robot and the validation with human participants. Then, the motor primitives classification results are illustrated and commented.

3.1. IMU-based estimation of upper-limb angles

3.1.1 ISB angles: validation on robotic arm

Figure 12 illustrates the results regarding the validation of the 5 ISB angles (*POE*, *AOE HR*, *FE*, *PS*), computed with IMU sensors and TIAGo's encoders during the execution of Test 2.

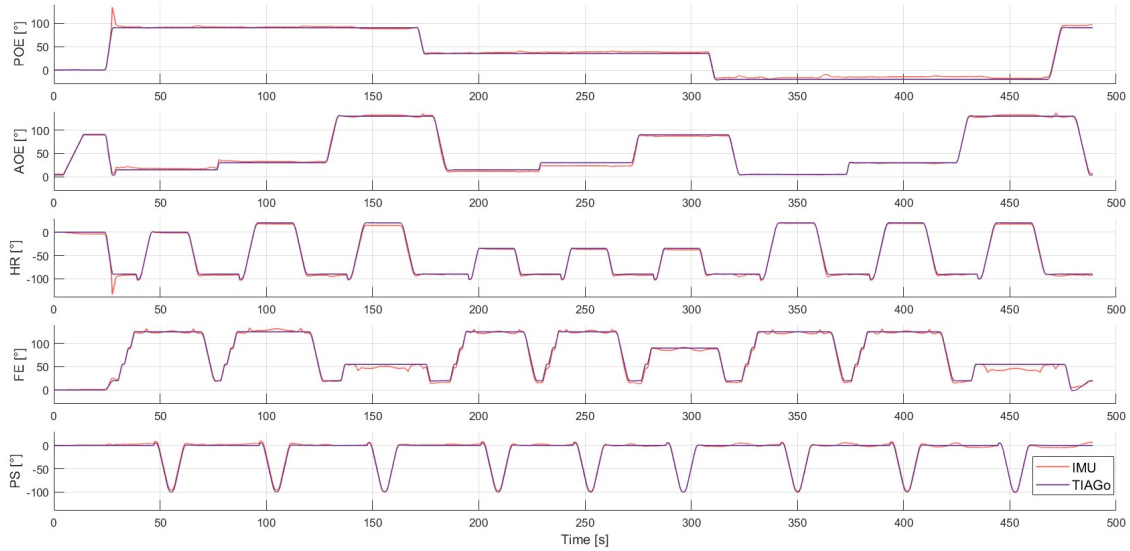

Figure 12: Upper limb joint angles measured by the encoders and estimated with the proposed method during the execution of Test 2. IMU angles are shown in orange, while angles coming from TIAGo's encoder are shown in blue.

From this figure, it is possible to notice that the two methods achieved very similar outcomes. However, in the first part of the acquisition, is possible to observe two pronounced peaks, a positive one for the *POE* and a negative one for the *HR*, in which the values relative to the IMUs and the robot's encoders are not correspondent. This discrepancy can be explained because of the *POE*'s computation method: this angle is in fact determined by the projection of the y-axis of UA onto the horizontal plane of TH. In the case of a very small *AOE* the definition of *POE* is ill-posed. Errors in the definition of the *POE* are directly transferred to the *HR* , given the direct relationship that links these two angles (Eq:14).
In Table 2, the results of the two tests (Test 1 and Test 2) in terms of RMSE, RMSE% relative to the ROM, and correlation coefficient ('r') are presented.

	Test 1			Test 2		
	r	RMSE [°]	RMSE[%]	r	RMSE [°]	RMSE[%]
POE	0.998	3.99	3.57	0.998	5.75	5.14
AOE	0.998	3.16	2.48	0.999	2.33	1.83
HR	0.999	3.23	2.67	0.999	2.27	1.87
FE	0.997	4.57	3.61	0.995	5.28	4.16
PS	0.997	2.54	2.41	0.993	7.37	6.99

Table 2: Correlation coefficient (r) and RMSE between TIAGO's encoders and IMU during two tests. RMSE% refers to the percentage of the RMSE with respect to the range of motion (ROM).

The observable correspondence between the two graphs (Figure 12) is further supported by the high correlation values in Table 2. The proposed algorithm effectively estimated TIAGo's joint angles by achieving an average error below 5° [45] and correlation coefficients always above 0.993. Errors for *POE* are slightly worse concerning the other shoulder angles: these errors can be explained, as mentioned earlier, with the ill-posed definition of this angle when *AOE* is near 0°. The results show similar metrics for Test 1 and Test 2. However, the angles of the elbow during Test 2 exhibit slightly higher errors and lower correlations compared to the one of Test 1. This might be explained by the introduction of inaccuracies during the calibration procedure.

3.1.2 ISB angles: validation on healthy participants

In this section, the results concerning the validation of the IMU-based angle extraction on 5 healthy participants are presented. A comparison between the angles computed using the IMUs and the optoelectronic system during the execution of tasks focused on exploring one angle at a time is presented.
To ensure the absence of offset-dependent errors, which can be caused, for instance, by different settings between the two systems, the mean was subtracted from all the signals. Table 3 displays the mean and standard deviation values of the differences between the mean of each signal provided by the optoelectronic system and the correspondent one computed with IMU data. For each angle, only the corresponding task was considered for the purpose to conduct the statistical analysis.

	Mean [°]	SD [°]
POE	22,724	21,716
AOE	11,014	4,255
HR	23,576	52,503
HR_{corr}	23,621	44,974
FE	-12,765	8,437
PS	73,022	26,504
PS_{corr}	69,686	36,944

Table 3: Average and standard deviation (SD) of the mean between subjects

As it is possible to observe from the first column depicted in Table 3, the mean differences between the two signals are quite different for all the angles. Similarly, the values of the standard deviation suggest that the offsets were quite different also among the subjects. The smallest values of both mean and standard deviation are the ones related to the *AOE* and *FE*. These two angles, in fact, were computed by the comparison of the orientation of the y-axes between consecutive segments and, since drift usually manifests as a deviation of the yaw angle, which is a rotation around the y-axis, is reasonable to infer that there could be a correlation between the variability of the offsets and drift. Moreover, is not always clear where the zero points of the optoelectronic system are located.
For the following results, the statistical analysis was conducted considering zero-mean signals.
Figure 13 represents the results obtained during the execution of single-angle tasks by one single subject for a time window of 20 seconds.

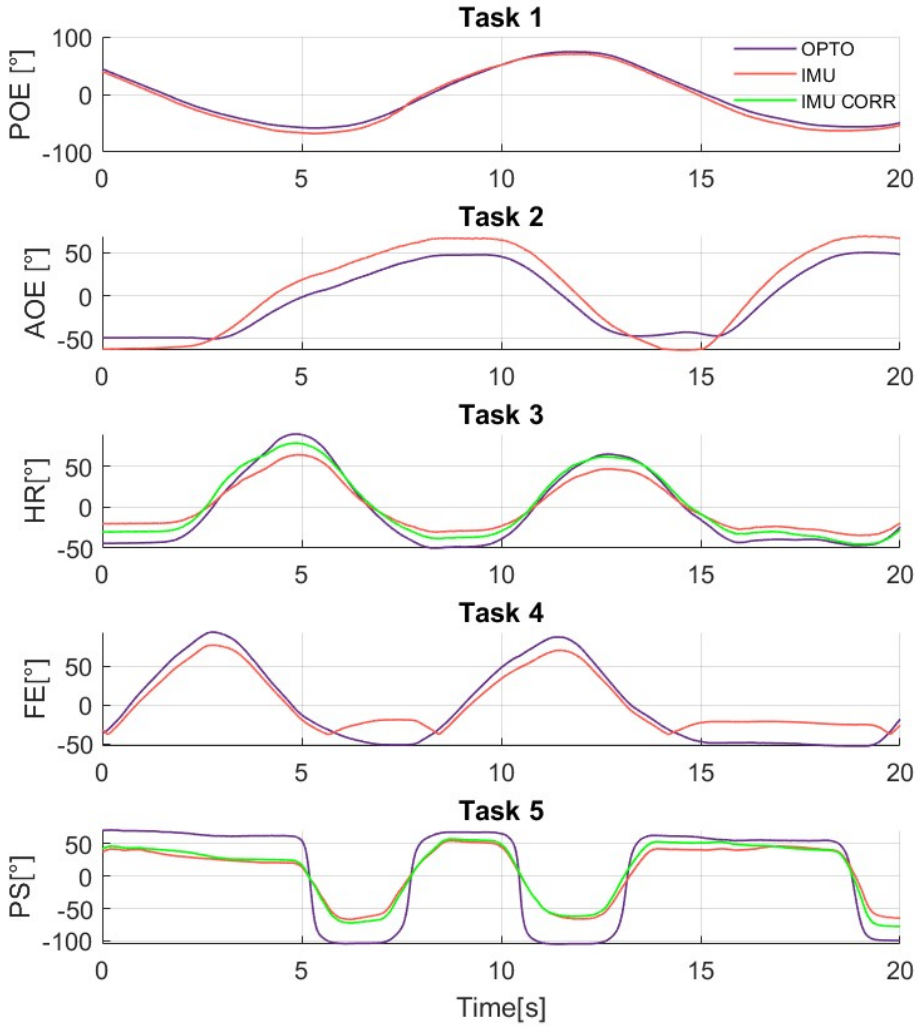

Figure 13: Shoulder angles (POE, AOE HR , HR_{corr}) for subject 1. The first plot from the top refers to the POE angle evaluated during Task 1, the second plot represents AOE during the execution of Task 2, while the third plot represents HR and HR_{corr} acquired during Task 3. The fourth and fifth plots from the top are relative to the FE and PS and PS_{corr} respectively. Red lines are relative to the angles computed without correction with IMUs, green refers to the IMU-based angles computer with UA correction, and the blue ones represent the angles extracted by the optoelectronic system

In Figure 13, the angles computed by means of the optoelectronic system and IMUs are represented. In particular, green plots refer to the angles registered with the IMUs and estimated by means of the correction of UA (UAcorr) presented in 2.1.5.
From Figure 13 it is possible to notice that there is an observable correlation between the IMU and optoelectronic angle. However, it is evident that for small values of AOE the curve related to the optoelectronic system measure reverses its concavity unlike the one related to IMU. This phenomenon can be attributed to two factors. The first is that the AOE computed by the IMUs, by definition, cannot invert signs when the 0 value is overcome. The second reason can be attributed to errors introduced by different 0° references between the two systems and by calibration: during the N-pose, in fact, the non-perfect alignment of the upper arms to the vertical axis due to hips width introduces an offset. However, by looking at the ROM of AOE it seems that the IMUs better estimated the actual AOE: indeed, the execution of Task 2 required the arm to explore the entire range of motion, ideally from 0° to 180° but the ROM of AOE estimated by the optoelectronic system is about 100°. HR_{corr} performed better than HR . The estimation of the latter angle was probably corrupted by the movements of soft tissues around the humerus. The correction allowed the definition of a rotation matrix for UA that moves, theoretically, in unison with the bone.
Consideration can be made about FE angle: the reversion of concavity of the curve associated with IMUs can

be attributed to the fact that these sensors do not differentiate between flexion and hyperextension of the elbow. Therefore, if the two systems had different 0° references, in the case of a complete extension one could read a hyperextension which is described as an angle >0°. It is possible to notice that the range of motion of *PS* and PS_{corr} is reduced for IMU measures with respect to the optoelectronic system. It is possible, in fact, that FA sensors, which were in a more proximal position compared to the wrist markers, rotated less in relation to them. The forearm Velcro bending could also have contributed to this effect. Moreover, the estimation of these angles can be biased by a drift, expected to cause an offset, or by a non-negligible ulnar deviation.
In Table 4, the RMSE, RMSE%, and r of 5 participants are summarized.

	RMSE[°]	RMSE%	r
POE	9,459 ±5, 270	6,525 ±3, 538	0,976 ±0, 028
AOE	16,000 ±4, 069	14,004 ±3, 674	0,952 ±0, 031
HR	15,365 ±3, 318	11,342 ±2, 373	0,963 ±0, 037
HR_{corr}	9,455 ±4, 380	7,303 ±3, 859	0,966 ±0, 032
FE	24,984 ±10, 932	16,397 ±7, 897	0,970 ±0, 019
PS	28,409 ±8, 239	16,905 ±3, 866	0,958 ±0, 022
PS_{corr}	29,654 ±12, 726	18,091 ±8, 802	0,919 ±0, 121

Table 4: Mean and standard deviation of RMSE, RMSE% evaluated on the range of motion (ROM) and correlation coefficients among 5 subjects.

As it can be seen in Figure 13, the mean and standard deviation values further confirm that *POE* is the angle with the most accurate estimation. The improvement of the *HR* estimation by the application of the correction is evident by observing RMSE values: a reduction of approximately 6° is observable between the corrected and uncorrected values. The correction can therefore compensate for the relative movement between UA sensor and the humerus caused by soft tissues.
The elbow joint exhibits significant RMSE. Nevertheless, the r values are comparable to the ones of the shoulder angles. Regarding the *FE* angle, as depicted in Figure 13, the curves have a similar trend but the IMU value are generally lower. This can be attributed to the offset present in FA estimation and the limitation that the *FE* angle cannot reach negative values.
The following plots represent the Bland-Altman plots for each angle and each participant (P1, P2, P3, P4, P5), representing the average and difference between two measurements respectively on the x-axis and y-axis.
Figure 14 depicts the Bland-Altman plot for the POE.

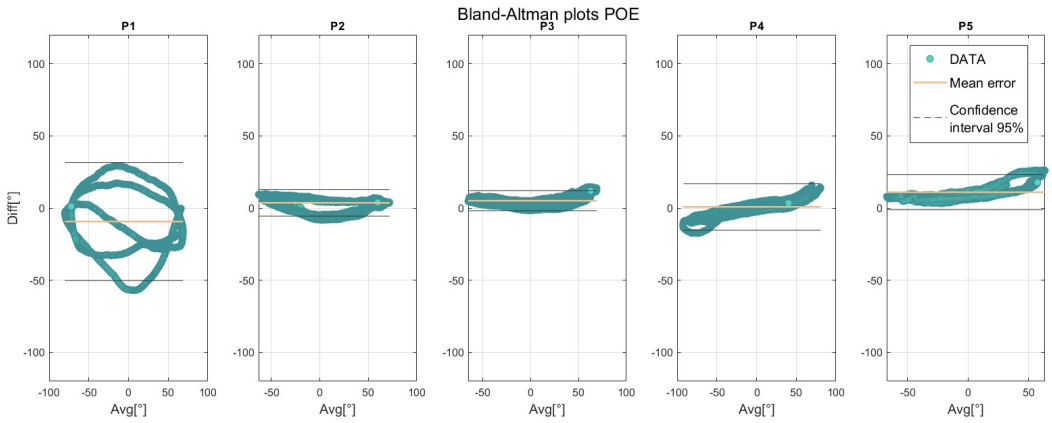

Figure 14: *POE* Bland-Altman plot for each participant during the execution of Task 1.

Except for the first participant (P1), the distribution of points is mainly horizontal and centered around the mean error. P2, P3, and P4 exhibit average error values near 0°. Regarding subject P4, the pattern of the distribution of points suggests that there was a correlation between the average *POE* and the difference between the two measurement systems.
The following figure represents the Bland-Altman plot for the AOE.

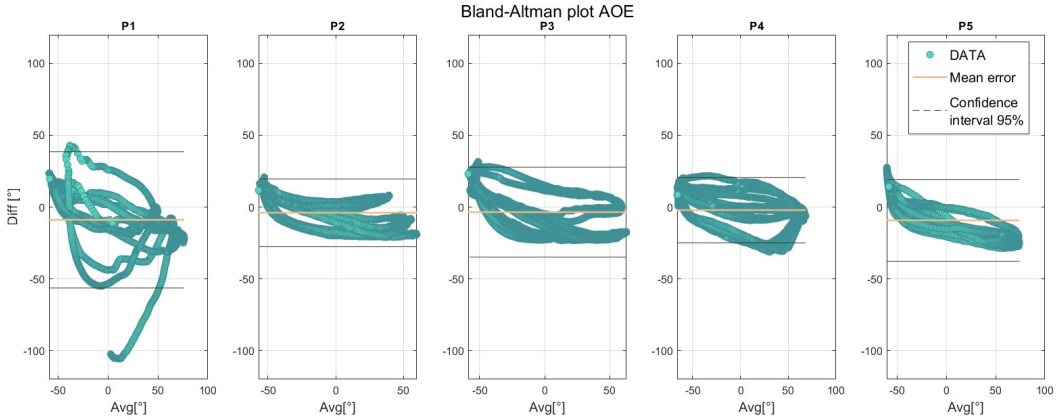

Figure 15: AOE Bland-Altman plot for each participant during the execution of Task 2.

Similarly to the *POE* the distribution of points for the *AOE* of P1 is more scattered with respect to the other subjects. For P3, P4, P5, and P6 the point mainly cluster around the mean error line (orange). However, they are more scattered with respect to *POE*: they exhibit wider ranges of values on the y-axis which are coherent with the higher mean RMSE illustrated in Table 4. Indeed, the RMSE for the *POE* was 9.46, while the one for the *AOE* was 15.99. Moreover, the inversion of concavity observable in Figure 13 manifests in the Bland-Altman plots as a peak towards high error for a small average of the signal.
Figure 16 and Figure 17 presented below depict the Bland-Altman plot for *HR* and HR_{corr}.

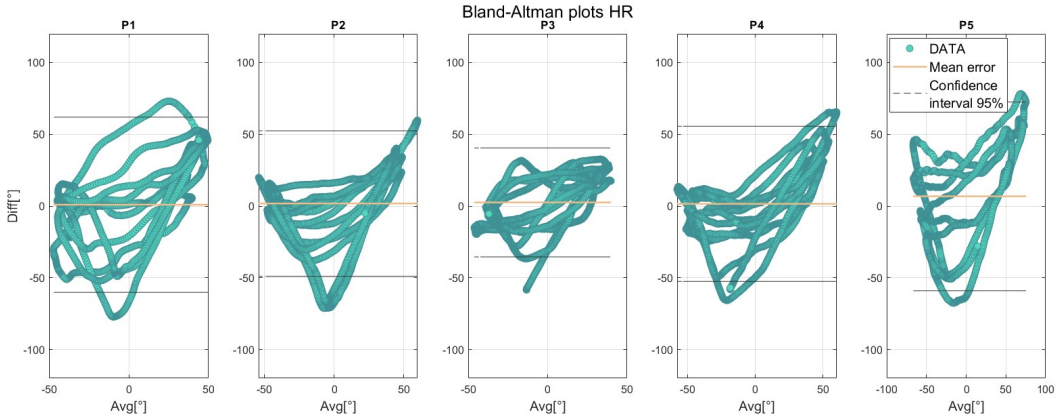

Figure 16: *HR* Bland-Altman plot for each participant during the execution of Task 3.

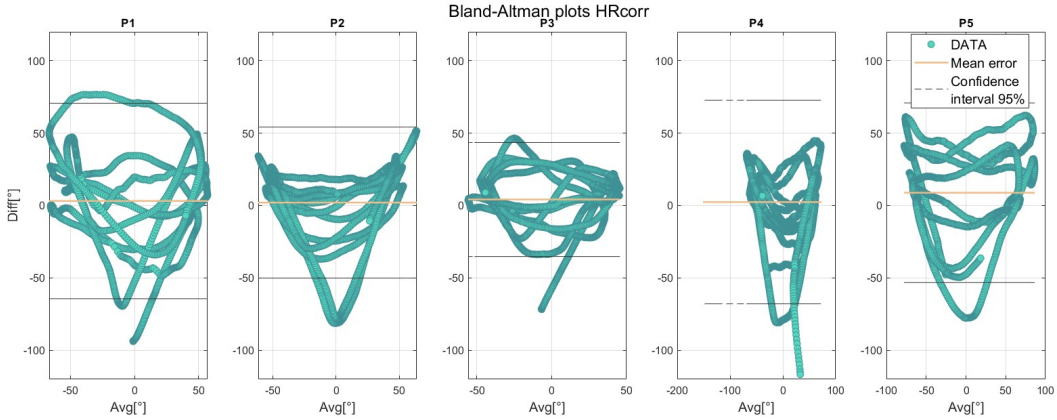

Figure 17: HR_{corr} Bland-Altman plot for each participant during the execution of Task 3.

For the *HR* and HR_{corr} angles, the pattern of distribution of points is not clear. However, is possible to observe that in general, the error increases at both the high and low extremities. This suggests that the error between

the two measurement systems is proportional to the average of the two signals. No particular differences between HR and HR_{corr} plots are detected.
The Bland-Altman plot for FE is depicted below.

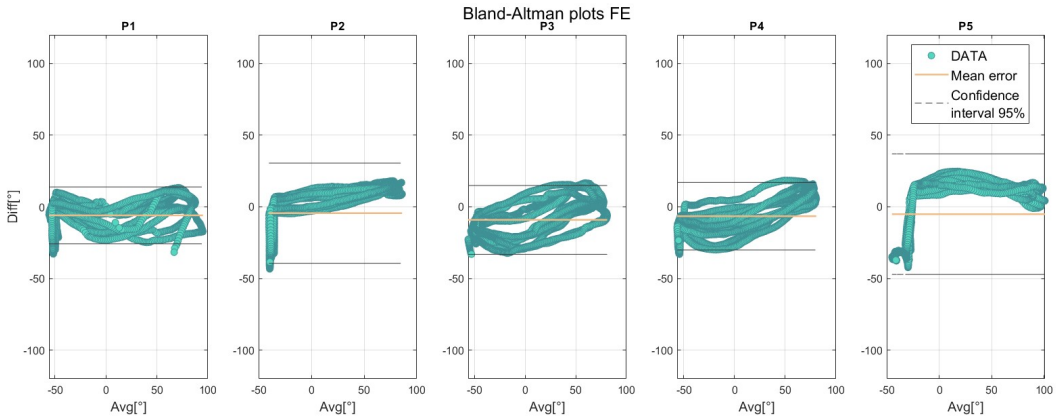

Figure 18: FE Bland-Altman plot for each participant during the execution of Task 4.

The Bland Altman plot for FE angle shows that the distribution of points is mainly horizontal. For P1, P2, and P3, and less evidently for P3 and P4, it's possible to observe a vertical distribution of points toward negative values of errors. As already noticed before, at small FE values, the signals obtained through optoelectronic and IMU systems exhibit opposite concavities. The definition of FE, in fact, is such that when the value overcomes 0°, the signal changes its concavity because the angle cannot assume negative values. The error in FE may be due to the fact that PS, in the case of the human body, is not a perfect rotation around the y-axis.

Finally, the Bland-Altman plots relative to PS and PS_{corr} are presented.

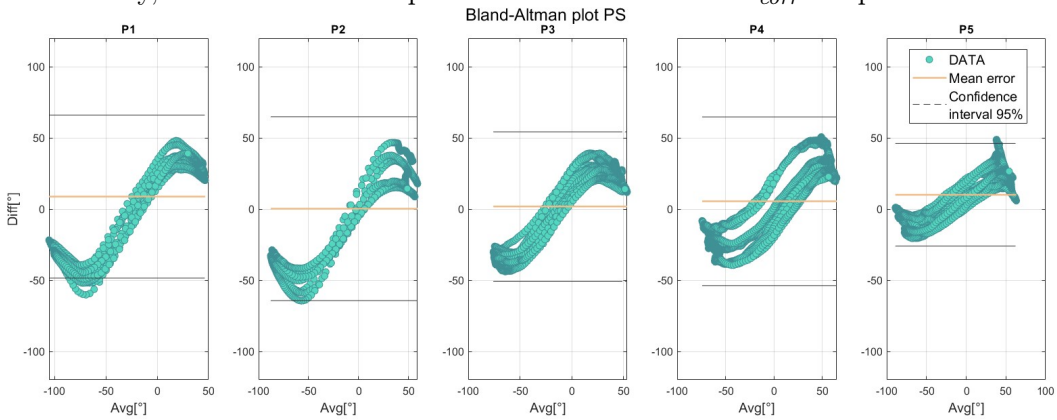

Figure 19: PS Bland-Altman plot for each participant during the execution of Task 5.

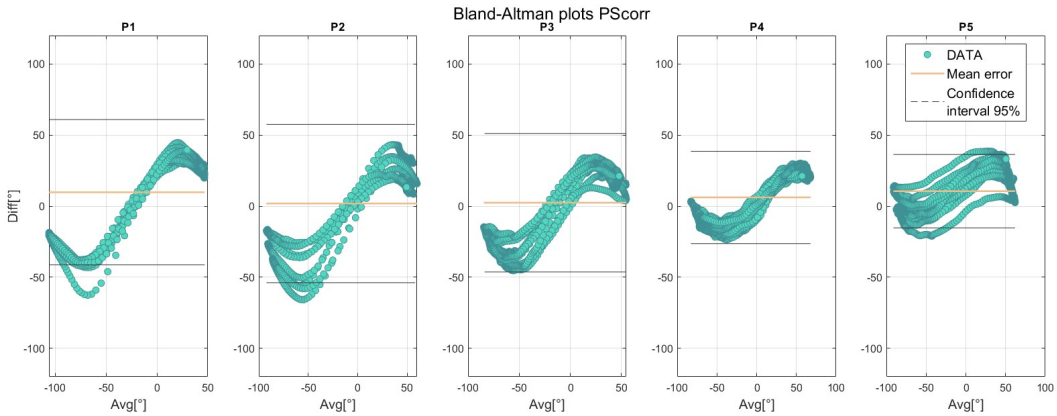

Figure 20: PS_{corr} Bland-Altman plot for each participant during the execution of Task 5.

By observing Figure 19 and Figure 20 is clear that there is a correlation between errors and signal average values. The Bland-Altman plot for PS and PS_{corr} confirms that IMU overestimates and underestimates respectively small values and high values of the pronation/supination angle. This effect could be due to the relative movement of the IMU placed on the forearm with respect to the segment itself: the velcro wristband, in fact, may displace from the initial position during forearm rotation. Moreover, the markers for the optoelectronic system were placed on the bony prominences of the wrist, while the IMU was positioned more proximally causing a lower sensitivity to rotations.
In summary, the best values were those relative to the POE both in terms of correlation, RMSE, and distribution of points in the Bland-Altman plot. These good results can be attributed to the orientation of UA during Task 1: the AOE was in fact around 90°, that is the configuration in which the projection of the y-axis of UA on the horizontal plane of TH is maximized. The Bland-Altman plots (Figure 15 and Figure 18) and the temporal trend of the angles suggest that the errors are mainly caused by the inversion of concavity. For what concerns the PS and PS_{corr}, the errors appear to be systematic errors.

3.2. Classification of motor primitives

In the following sections, the results for different LSTM complexity trained with different dataset combinations are presented. Each combination was repeated 5 times and for each repetition, the dataset was shuffled but still maintaining the temporal order of samples within a single exercise. This approach ensures that the validation set varies for each repetition. The f1-scores obtained during testing phases were averaged over 5 repetitions for each combination of LSTM depth and datasets.

3.2.1 Primitives classification: dataset A

The table below depicts the values of training f1-scores for various depth settings (50, 100, 200, 300) of the LSTM layer. During this first experiment, these models were trained and tested using only the SADL dataset (dataset A).

Training dataset A

LSTM DEPTH	50	100	200	300
Absolute	0,584 ±0, 061	0,834 ±0, 006	0,871 ±0, 007	0,886 ±0, 012
Idle	0,885 ±0, 003	0,897 ±0, 004	0,909 ±0, 004	0,916 ±0, 006
Stabilize	0,725 ±0, 308	0,889 ±0, 006	0,900 ±0, 008	0,893 ±0, 042
Reach	0,634 ±0, 017	0,722 ±0, 013	0,787 ±0, 014	0,822 ±0, 019
Transport	0,428 ±0, 204	0,865 ±0, 005	0,897 ±0, 005	0,911 ±0, 008
Reposition	0,690 ±0, 002	0,751 ±0, 010	0,818 ±0, 011	0,839 ±0, 006

Table 5: Training f1 scores (mean and standard deviation for dataset A (SADL) averaged over 5 repetitions in which validation set was chosen randomly among training dataset.

As it is possible to observe from 5, LSTM50 is the model that achieved the lower f1-scores during the training phase. Moreover, the variability of the performance of this model is high compared to the other one: this means that the model is less robust with respect to the other, and the accuracy of the classification depends on the set of data used for training and validation. In general, the f1-score increase directly with the model depth.
The following table represents the values of f1-score achieved during the testing phase of dataset A.

Testing dataset A

LSTM DEPTH	50	100	200	300
Absolute	0,738 ±0, 006	0,754 ±0, 005	0,765±0, 006	0,762±0, 008
Idle	0,855 ±0, 008	0,856 ±0, 008	0,862 ±0, 005	0,855 ±0, 010
Stabilize	0,779 ±0, 015	0,778 ±0, 023	0,789 ±0, 019	0,794 ±0, 018
Reach	0,544 ±0, 042	0,612 ±0, 010	0,621 ±0, 016	0,623 ±0, 014
Transport	0,784 ±0, 005	0,797 ±0, 007	0,808 ±0, 005	0,802 ±0, 008
Reposition	0,590 ±0, 007	0,628 ±0, 013	0,651 ±0, 005	0,649 ±0, 015

Table 6: Testing f1 scores (mean and standard deviations) for dataset A averaged over 5 repetitions in which validation set was chosen randomly among training dataset.

Considering that the f1-score is a value between 0 and 1, in which 1 represents the best performance in terms of precision and recall, it can be stated that LSTM200 performed better compared to the other model. By looking at the overall ('Absolute') f1-scores, in fact, LSTM200 has the highest value (0.765), followed closely by LSTM300 (0.762). The observed lack of improvement in training performance from LSTM200 to LSTM300 suggests potential overfitting due to the limited dataset size and the excessive model complexity.
The performance varies across different primitives: the best results were achieved by 'idle', and 'transport' primitives since their f1-score was respectively 0.862, 0.808 for LSTM200. 'Stabilize' class also achieved an f1-score of 0.789 for LSTM200, which is worthy of note since this primitive is characterized by a kinematic similar to the one of 'idle' primitive. The variation in f1-scores can be attributed to the dataset's imbalance toward 'transport' and 'idle' classes. The SD is low for all models, with the highest value beign the 'reach' class for LSTM50.
The following figure represents the confusion matrix for LSTM200 model trained and tested with dataset A during one repetition. The diagonal values represent the sensitivity for each primitive, which is representative of how often the model predicted correctly a primitive.

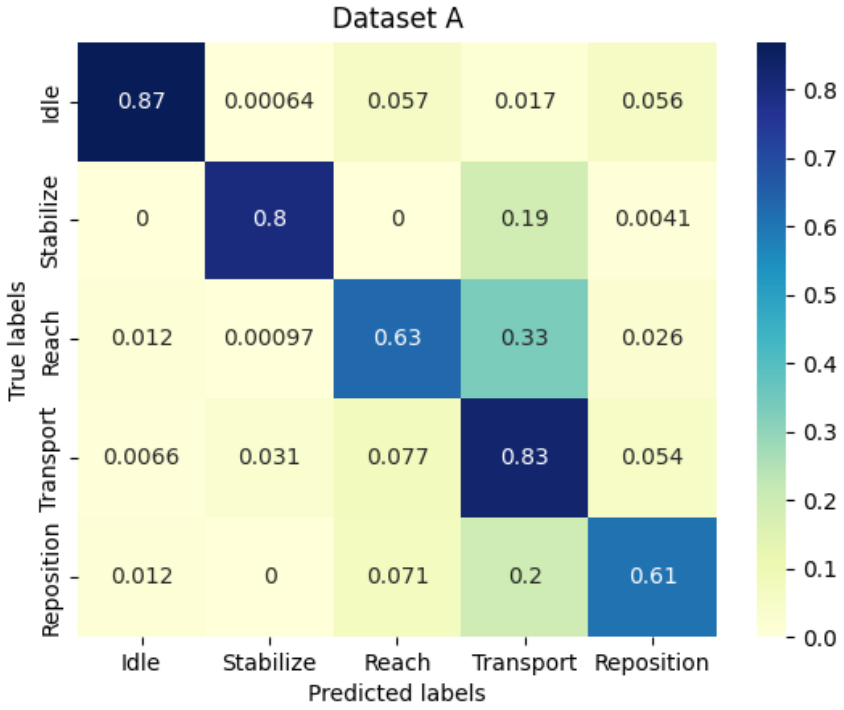

Figure 21: Confusion matrix for LSTM200 trained and tested only with data from SADL dataset.

The confusion matrix further describes the performance of the model by providing a comparison between predicted labels and true labels. By looking at Figure 21, a consideration can be done: stabilization often occurs between two transports and in CADL scenario it was not always easy to recognize the boundary between two primitives. Moreover, it is possible to notice that the misclassification of 'reach' and 'reposition', was mainly in favor of the 'transport' class. This result is reasonable since the dataset contains more windows labeled as 'transport' than one of the other classes. Moreover, this primitive includes a variety of movements that can be similar to the ones of 'reach' and 'reposition' since the models had no information regarding the kinematics of the hand.

3.2.2 Primitives classification: Dataset B

The table below depicts the training f1-score of different LSTM models trained and tested with both CADL and SADL data (dataset B).

Training dataset B

LSTM DEPTH	50	100	200	300
Absolute	0,474 ±0, 112	0,757 ±0, 011	0,791 ±0, 034	0,812 ±0, 008
Idle	0,582 ±0, 380	0,870 ±0, 017	0,890 ±0, 008	0,894 ±0, 005
Stabilize	0,791 ±0, 022	0,820 ±0, 021	0,849 ±0, 013	0,857 ±0, 010
Reach	0,348 ±0, 050	0,510 ±0, 033	0,594 ±0, 028	0,652 ±0, 020
Transport	0,405 ±0, 288	0,827 ±0, 006	0,812 ±0, 082	0,860 ±0, 005
Reposition	0,517 ±0, 040	0,605 ±0, 034	0,685 ±0, 013	0,731 ±0, 008

Table 7: Training f1 scores (mean and standard deviation) for dataset B averaged over 5 repetitions in which validation set was chosen randomly among training dataset.

Similarly to dataset A, the model performance during the training phase increases with LSTM depth. Also with dataset B, LSTM50 shows a higher variability in f1-score across the 5 repetitions.
The following table represents the testing f1-score of different LSTM models trained and tested with both CADL and SADL data (dataset B).

Testing dataset B

LSTM DEPTH	50	100	200	300
Absolute	0,700 ±0, 003	0,714 ±0, 005	0,711 ±0, 005	0,718 ±0, 002
Idle	0,824 ±0, 018	0,828 ±0, 013	0,823 ±0, 012	0,827 ±0, 012
Stabilize	0,654 ±0, 024	0,663 ±0, 017	0,679 ±0, 017	0,674 ±0, 008
Reach	0,335 ±0, 026	0,431 ±0, 011	0,487 ±0, 017	0,485 ±0, 013
Transport	0,778 ±0, 001	0,784 ±0, 004	0,777 ±0, 004	0,784 ±0, 004
Reposition	0,445 ±0, 023	0,535 ±0, 017	0,550 ±0, 026	0,566 ±0, 009

Table 8: Testing f1 scores (mean and standard deviation) for dataset B averaged over 5 repetitions in which validation set was chosen randomly among training dataset.

The classification performance is still good for 'idle' and 'transport' primitives. However, it is possible to notice that the f1-score decreased for the other classes. CADL dataset introduced variability since the movements during CADLs were faster and the participants in the acquisition protocol were free to move in the space as they wished. The absolute f1-score increases with model depth: increasing the model's complexity in fact, the algorithm could learn more complex representations.
The following figure represents the confusion matrix for LSTM200 model trained and tested with dataset B during one repetition.

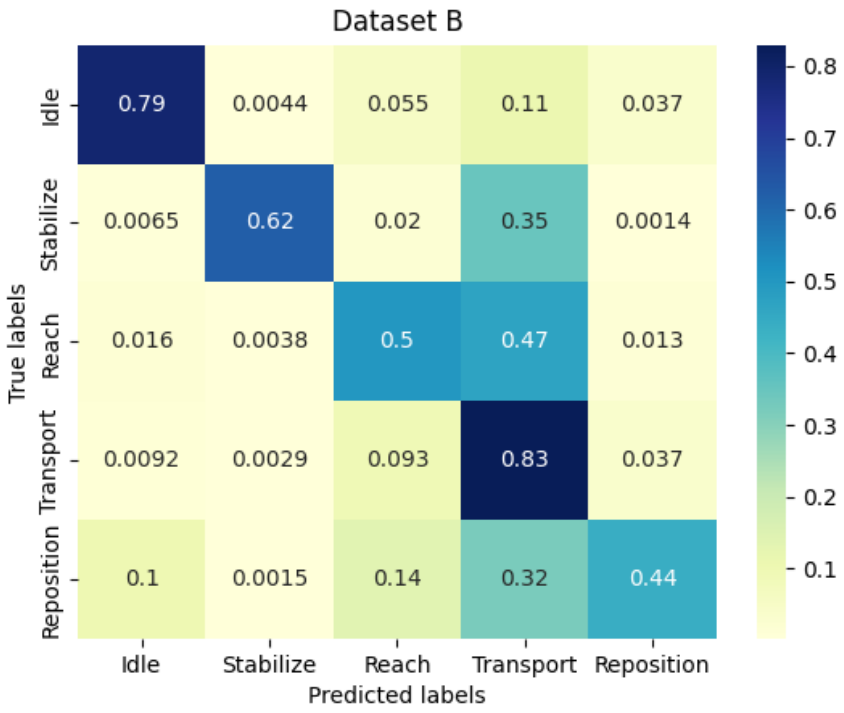

Figure 22: Confusion matrix for LSTM200 trained and tested with data from dataset B.

As for 3.2.1, from the confusion matrix is possible to notice that the misclassifications were mainly in favor of the 'transport' class. Moreover, 'stabilize' primitive was well distinguished from 'idle' class.
Results for different LSTM depths with different datasets show that by training the algorithm with only SADL exercises, the performance is increased. In particular, the main difference can be observed in the classification of 'reach' movements. This result was predictable since in SADL dataset acquisition, the same exercises have been executed in the same way for all participants. On the contrary, some variability has been introduced in the CADL activities, in which subjects were able to move as they wished and the density of primitives over time was generally higher with respect to SADL. The same consideration cannot be made for 'reach' classification in ADL dataset. From Table 7 is possible to observe that the f1-score for 'reach' class is better for a depth of 200 with respect to 300. This behavior suggests that increasing the complexity of the model for the ADL dataset caused an overfitting effect. Datasets were, in fact, unbalanced, with a prevalence of 'transport' class compared to the others.

4. Conclusions and future developments

The aim of this thesis is to build the foundation for future works based on the upper limb kinematic analysis of exosuits users. The final application is twofold: on the one side, upper limb kinematics will be used for gravity compensation control, on the other side, it will be exploited to assess and monitor the user's motor performance progress to provide feedback and sustain engagement.
The first phase of this project was focused on developing an algorithm to compute upper limb joint angles defined according to the ISB convention from a set of 3 IMUs. To this purpose, a three-step magnetometer-free calibration procedure, which allows a free-positioning of the sensors on the body segments, was defined.
A first validation of the algorithm to extract ISB angles from the IMU system was conducted using the TIAGo robot, comparing the angles computed with the ones read by the encoders of the robot's motors. This validation led to excellent results, with errors ranging overall between 2.33° to 7.37° and correlation coefficients above 0.993.
A second validation was conducted on 5 healthy participants whose arm joint angles were simultaneously recorded with the IMUs and an optoelectronic system that captured markers placed on bony prominences. A correction was applied to *HR* and *PS* (see 2.1.5) in order to compensate for soft tissue movement around the humerus. The data acquired with the optoelectronic and the IMU-based systems were then compared by means of RMSE and correlation coefficient. The best results considering all the participants were achieved for *POE* and HR_{corr} (RMSE<10°). Results also confirmed that the correction applied to *HR* and *PS* effectively mitigated the effect of soft tissue-bone relative movement (HR_{corr} RMSE<10°). Correlation coefficients were above 0.91

for all the angles. Higher errors were computed for the *AOE* (average RMSE of 16°). However, considering that during the execution of Task 2, the arm should have been raised to its maximum, is plausible to think that the IMUs would be more accurate since they estimated a wider ROM. Regarding the *FE*, by looking at Figure 13 is possible to notice an inversion of concavity of the IMU plot. Since the metrics have been evaluated after removing the mean of the signal, the errors might appear larger than the actual discrepancy. The poor results achieved for *PS* and PS_{corr} are related to the underestimation of the IMUs probably due to the relative movement of the wristband and the more proximal position of FA sensor with respect to the wrist markers.
Furthermore, even if the optoelectronic system is commonly used for assessing upper limb movements, it is important to note that nowadays, there is not a universally accepted standard for UL kinematic assessment and that some errors could have been induced by this system itself.
The second phase of this work focused on the classification of motor primitives starting from the angles extracted with the previously described algorithm, angular velocities, and linear accelerations by means of LSTM neural networks. The results obtained by training and testing LSTM200 and LSTM300 using only the SADL dataset show that 'idle', 'stabilize', and 'transport' were classified with a fairly good test f1-score of approximately 0.8, which represents a reasonable balance between precision and recall. Furthermore, even if 'idle' and 'stabilize' are characterized by very similar kinematics since the arm is practically stationary, is interesting to notice from Figure 21 that they have been clearly distinguished. The classes of 'reach' and 'reposition' were instead misclassified mainly as 'transport'. This outcome was predictable since the dataset was highly imbalanced toward this class and, moreover, 'transport' includes movements that can be very similar to the one of 'reach' and 'reposition' if the hand's kinematic is not considered.
To test the capability of the LSTM model to classify primitives acquired in an ADL setting, the model underwent training and testing using data from both SADL and CADL datasets. CADL movements are in fact faster and more variegated with respect to the SADL ones. Moreover, during the acquisition of CADL movements, the participant was moving freely around the space, which made the labeling process more challenging. As expected, the test f1-scores obtained with these models were lower with respect to the first model but still achieved an overall f1-score of 0.73 for LSTM300 tested on SADL and CADLs. Also in this scenario, the primitives that were better classified were 'idle' and 'transport', while 'stabilize' f1-score decreased due to a significant portion being misclassified as 'transport'. Also 'reach' and 'reposition' primitives were mainly misclassified as 'transport'. As stated before, this classification error can be justified by the lack of information regarding the grasping movement of the hand.
The performance of the algorithm was lower with respect to other studies aimed at the classification of the primitive. Nevertheless, it is important to acknowledge that in this study, a smaller number of IMUs (3 in this study compared to the 7 in [36] and 9 in [37]) was used. This simplification is necessary to translate research in the final application that will be in an assistive scenario, where the exosuit must ensure maximum comfort while minimizing the complexity of the device. Additionally, in this work, the classification relies on a reduced set of input features (26 compared to 77 [37] and 665 [36]) which can be an advantage in terms of robustness and generalization ability.
Considering these factors, it is reasonable to view this work as an initial milestone toward the broader objective of integrating functional movement assessment into exosuits for daily assistance. The promising outcomes achieved through robot validation, coupled with the recognition of potential factors contributing to errors in human validation, instill confidence that, by adding proper user-specific parameters, like ulnar deviation and hip width, the proposed method can become operational and successfully implemented. Further research could also be conducted to estimate drift, thus allowing the reliability of the measure within long periods of time. Moreover, the inclusion of activities of daily living did not result in a significant deterioration of the algorithm's performance. This finding highlights the feasibility of classifying primitives in an uncontrolled environment, paving the way for broader applicability and real-world deployment. As previously mentioned, in both models, a part of this misclassification could be attributed to dataset imbalance and inaccurate data labeling. To improve classification performance, it is advisable to use a more wider and balanced dataset and ensure accurate labeling by capturing videos at a higher frames-per-second rate, while also cross-checking for potential labeling errors. Moreover, algorithm performance could also be enhanced by adding a fourth sensor on the hand as long as it is compatible with the wearability of the exosuit.

References

[1] Shu-Ya Chen and Carolee J. Winstein. A systematic review of voluntary arm recovery in hemiparetic stroke. *Journal of Neurologic Physical Therapy*, 33(1):2–13, mar 2009.

[2] Samar M. Hatem, Geoffroy Saussez, Margaux della Faille, Vincent Prist, Xue Zhang, Delphine Dispa, and Yannick Bleyenheuft. Rehabilitation of motor function after stroke: A multiple systematic review focused on techniques to stimulate upper extremity recovery. *Frontiers in Human Neuroscience*, 10, 9 2016.

[3] Mindy F. Levin, Jeffrey A. Kleim, and Steven L. Wolf. What do motor "recovery" and "compensation" mean in patients following stroke? *Neurorehabilitation and Neural Repair*, 23(4):313–319, dec 2008.

[4] Mark V. W. Morris D. M. Taub E., Uswatte G. The learned nonuse phenomenon: implications for rehabilitation. 2006.

[5] Gert Kwakkel, Roland van Peppen, Robert C. Wagenaar, Sharon Wood Dauphinee, Carol Richards, Ann Ashburn, Kimberly Miller, Nadina Lincoln, Cecily Partridge, Ian Wellwood, and Peter Langhorne. Effects of augmented exercise therapy time after stroke. *Stroke*, 35(11):2529–2539, nov 2004.

[6] David Gladstone, Cynthia Danells, and Sandra Black. The fugl-meyer assessment of motor recovery after stroke: A critical review of its measurement properties. 2002.

[7] Ching-Fan Sheu Jau-Hong Lin, I-Ping Hsueh and Ching-Lin Hsieh. Psychometric properties of the sensory scale of the fugl-meyer assessment in stroke patients. 2004.

[8] Won Hyuk Chang and Yun-Hee Kim. Robot-assisted therapy in stroke rehabilitation. *Journal of Stroke*, 15(3):174, 2013.

[9] Belén Rubio Ballester, Alica Lathe, Esther Duarte, Armin Duff, and Paul F M J Verschure. *A Wearable Bracelet Device for Promoting Arm Use in Stroke Patients.*

[10] Valeria Longatelli, Alberto Antonietti, Emilia Biffi, Eleonora Diella, Maria Grazia D'Angelo, Mauro Rossini, Franco Molteni, Marco Bocciolone, Alessandra Pedrocchi, and Marta Gandolla. User-centred assistive SystEm for arm functions in neUromuscuLar subjects (USEFUL): a randomized controlled study. *Journal of NeuroEngineering and Rehabilitation*, 18(1), jan 2021.

[11] Hao Lee, Peter Walker Ferguson, and Jacob Rosen. Chapter 11 - lower limb exoskeleton systems—overview. pages 207–229, 2020.

[12] Elena Bardi, Marta Gandolla, Francesco Braghin, Ferruccio Resta, Alessandra L.G. Pedrocchi, and Emilia Ambrosini. Upper limb soft robotic wearable devices: a systematic review. *Journal of neuroengineering and rehabilitation*, 19, 12 2022.

[13] Maria C. De Cola Alessia Bramanti Placido Bramanti Rocco Salvatore Calabrò Rachele Bertani, Corrado Melegari. Effects of robot-assisted upper limb rehabilitation in stroke patients: a systematic review with meta-analysis. *Neurol Sci*, 2017.

[14] Ana C. De Oliveira, James S. Sulzer, and Ashish D. Deshpande. Assessment of upper-extremity joint angles using harmony exoskeleton. *IEEE Transactions on Neural Systems and Rehabilitation Engineering*, 29:916–925, 2021.

[15] Ashraf S Gorgey. Robotic exoskeletons: The current pros and cons. *World Journal of Orthopedics*, 9(9):112–119, sep 2018.

[16] Giacomo Zuccon, Matteo Bottin, Marco Ceccarelli, and Giulio Rosati. Design and performance of an elbow assisting mechanism. *Machines*, 8(4):68, oct 2020.

[17] Ciaran O'Neill, Tommaso Proietti, Kristin Nuckols, Megan E. Clarke, Cameron J. Hohimer, Alison Cloutier, David J. Lin, and Conor J. Walsh. Inflatable soft wearable robot for reducing therapist fatigue during upper extremity rehabilitation in severe stroke. *IEEE Robotics and Automation Letters*, 5(3):3899–3906, jul 2020.

[18] M Asgari. Wearable shoulder exoskeleton with spring-cam mechanism for customizable, nonlinear gravity compensation. IEEE, 2023.

[19] Nuray Yozbatiran, Lucy Der-Yeghiaian, and Steven C. Cramer. A standardized approach to performing the action research arm test. *Neurorehabilitation and Neural Repair*, 22:78–90, 1 2008.

[20] Anne Schwarz, MSc*; Christoph M. Kanzler, MSc*; Olivier Lambercy, PhD, Andreas R. Luft, MD, PhD; Janne M. Veerbeek, and PhD. Systematic review on kinematic assessments of upper limb movements after stroke. Technical Report Technology,, 2023.

[21] Gyrd Thrane, Torunn Askim, Roland Stock, Bent Indredavik, Ragna Gjone, Anne Erichsen, and Audny Anke. Efficacy of constraint-induced movement therapy in early stroke rehabilitation. *Neurorehabilitation and Neural Repair*, 29:517–525, 7 2015.

[22] Song Zhao, Yun su Chen, and Xian long Zhang. Clinical application of gait analysis in hip arthroplasty. *Orthopaedic Surgery*, 2(2):94–99, may 2010.

[23] Stefano Dalla Gasperina, Valeria Longatelli, Mattia Panzenbeck, Beatrice Luciani, Alice Morosini, Alessandro Piantoni, Peppino Tropea, Francesco Braghin, Alessandra Pedrocchi, and Marta Gandolla. AGREE: an upper-limb robotic platform for personalized rehabilitation, concept and clinical study design. In *2022 International Conference on Rehabilitation Robotics (ICORR)*. IEEE, jul 2022.

[24] Catherine E. Lang, Kimberly J. Waddell, Joseph W. Klaesner, and Marghuretta D. Bland. A method for quantifying upper limb performance in daily life using accelerometers. *Journal of Visualized Experiments*, 2017, 4 2017.

[25] Catherine E. Lang, Joanne M. Wagner, Dorothy F. Edwards, and Alexander W. Dromerick. Upper extremity use in people with hemiparesis in the first few weeks after stroke. *Journal of Neurologic Physical Therapy*, 31:56–63, 2007.

[26] Nguyen J. Samuelsson J. et al. Neishabouri, A. Quantification of acceleration as activity counts in actigraph wearable. *Sci Rep 12*, 2022.

[27] Ryan R. Bailey, Joseph W. Klaesner, and Catherine E. Lang. Quantifying real-world upper-limb activity in nondisabled adults and adults with chronic stroke. *Neurorehabilitation and Neural Repair*, 29(10):969–978, apr 2015.

[28] Inge van den Akker-Scheek Claudine J. C. Lamoth Mariano Bernaldo de Quirós, E.H. Douma and Natasha M. Maurits. Quantification of movement in stroke patients under free living conditions using wearable sensors: A systematic review. 2022.

[29] Kaspar Leuenberger, Roman Gonzenbach, Susanne Wachter, Andreas Luft, and Roger Gassert. A method to qualitatively assess arm use in stroke survivors in the home environment. *Medical and Biological Engineering and Computing*, 55:141–150, 1 2017.

[30] Sebastian Madgwick, Andrew Harrison, and Ravi Vaidyanathan. Estimation of imu and marg orientation using a gradient descent algorithm. In *2011 IEEE International Conference on Rehabilitation Robotics Rehab Week Zurich, ETH Zurich Science City, Switzerland, June 29 - July 1, 2011*. IEEE, 2011.

[31] Tanya Subash, Ann David, StephenSukumaran ReetaJanetSurekha, Sankaralingam Gayathri, Selvaraj Samuelkamaleshkumar, Henry Prakash Magimairaj, Nebojsa Malesevic, Christian Antfolk, Varadhan SKM, Alejandro Melendez-Calderon, and Sivakumar Balasubramanian. Comparing algorithms for assessing upper limb use with inertial measurement units. 13, dec 2022.

[32] Juan Pablo Gomez-Arrunategui, Janice J. Eng, and Antony J. Hodgson. Monitoring arm movements post-stroke for applications in rehabilitation and home settings. *IEEE Transactions on Neural Systems and Rehabilitation Engineering*, 30:2312–2321, 8 2022.

[33] Domitilla Del Vecchio, Richard M. Murray, and Pietro Perona. Decomposition of human motion into dynamics-based primitives with application to drawing tasks. *Automatica*, 39(12):2085–2098, dec 2003.

[34] Heidi M. Schambra, Avinash Parnandi, Natasha G. Pandit, Jasim Uddin, Audre Wirtanen, and Dawn M. Nilsen. A taxonomy of functional upper extremity motion. *Frontiers in Neurology*, 10(Munich,), aug 2019.

[35] Torricelli-D. Tornero J. et al Longatelli, V. A unified scheme for the benchmarking of upper limb functions in neurological disorders.

[36] Jorge Guerra, Jasim Uddin, Dawn Nilsen, James Mclnerney, Ammarah Fadoo, Isirame Omofuma, Shatif Hughes, Sunil Agrawal, Peter Allen, and Heidi Schambra. Capture, learning, and classification of upper extremity movement primitives in healthy controls and stroke patients.

[37] Avinash Parnandi, Aakash Kaku, Anita Venkatesan, Natasha Pandit, Audre Wirtanen, Haresh Rajamohan, Kannan Venkataramanan, Dawn Nilsen, Carlos Fernandez-Granda, and Heidi Schambra. PrimSeq: A deep learning-based pipeline to quantitate rehabilitation training. 1(6):e0000044, jun 2022.

[38] Ge Wu, Frans C.T. van der Helm, H.E.J. (DirkJan) Veeger, Mohsen Makhsous, Peter Van Roy, Carolyn Anglin, Jochem Nagels, Andrew R. Karduna, Kevin McQuade, Xuguang Wang, Frederick W. Werner, and Bryan Buchholz. ISB recommendation on definitions of joint coordinate systems of various joints for the reporting of human joint motion—part II: shoulder, elbow, wrist and hand. 38(5):981–992.

[39] Mahmoud El-Gohary and James McNames. Human joint angle estimation with inertial sensors and validation with a robot arm. *IEEE Transactions on Biomedical Engineering*, 62(7):1759–1767, jul 2015.

[40] Martina Lapresa, Christian Tamantini, Francesco Scotto di Luzio, Marco Ferlazzo, Gianfranco Sorrenti, Flavio Corpina, and Loredana Zollo. Validation of magneto-inertial measurement units for upper-limb motion analysis through an anthropomorphic robot. *IEEE Sensors Journal*, 22(17):16920–16928, sep 2022.

[41] Gandolla Marta, Ferrante Simona, Costa Andrea, Bortolotti Dario, Sorti Stefano, Vitale Federico, Bocciolone Marco, Braghin Francesco, Masiero Stefano, and Pedrocchi Alessandra. Wearable biofeedback suit to promote and monitor aquatic exercises: A feasibility study. *IEEE Transactions on Instrumentation and Measurement*, 69(4):1219–1231, 2020.

[42] Luca Pozzi, Marta Gandolla, Filippo Pura, Marco Maccarini, Alessandra Pedrocchi, Francesco Braghin, Dario Piga, and Loris Roveda. Grasping learning, optimization, and knowledge transfer in the robotics field. *Sci. Rep.*, 12(1):4481, 2022.

[43] George Rab, Kyria Petuskey, and Anita Bagley. A method for determination of upper extremity kinematics.

[44] Elena Bardi, Carola Butera, Luca Pozzi, Marta Gandolla, Francesco Braghin, and Emilia Ambrosini. 3D upper limbs tracking through inertial sensors : calibration , methodology , and validation. In *GNB 2023*, pages 1–4, Padova, Italy, 2023.

[45] Jennifer L. McGinley, Richard Baker, Rory Wolfe, and Meg E. Morris. The reliability of three-dimensional kinematic gait measurements: A systematic review. *Gait &amp Posture*, 29(3):360–369, apr 2009.

Abstract in lingua italiana

La qualità della vita di una persona colpita da un problema cronico agli arti superiori può essere compromessa in modo significativo. Per questa ragione, la riabilitazione motoria e l'assistenza nelle attività quotidiane (ADL) sono fondamentali. Nel contesto dell'assistenza domiciliare, gli esoscheletri rappresentano uno strumento valido per assistere i movimenti degli arti nell'esecuzione delle ADL grazie alla cooperazione tra sensori e attuatori. Questa tesi fa parte di un ampio progetto volto allo sviluppo di un esoscheletro per l'assistenza del movimento degli arti superiori. In particolare, tre sensori inerziali (IMU) sono integrati nel dispositivo per consentire la compensazione n tempo reale del peso del braccio dovuto alla gravità. L'idea alla base di questo lavoro è quella di sfruttare i sensori integrati per ricavare un modello cinematico da utilizzare per il controllo dell'esoscheletro e monitorare quotidianamente la funzionalità dell'arto superiore. In tal modo, le informazioni ricavate potrebbero essere utilizzate per fornire feedback e favorire il coinvolgimento dell'utente. A tal fine, sono stati definiti due obiettivi: i) implementare il calcolo online degli angoli anatomici in conformità allo standard dell'ISB (International Society of Biomechanics), ii) definire, addestrare e testare una rete neurale per la classificazione delle primitive motorie. Per raggiungere il primo obiettivo, è stata proposta una procedura di calibrazione in tre fasi (reset IMU, N-pose e T-pose). Successivamente, è stata completata la formalizzazione del metodo di calcolo per 5 angoli ISB, compresi il piano di elevazione (POE), l'angolo di elevazione (AOE), la rotazione dell'omero (*HR*), la flessione/estensione (FE) e la pronazione/supinazione (*PS*),. Inoltre, è stato sviluppato un metodo di correzione per HR e *PS* al fine di compensare il movimento relativo dei sensori del braccio superiore rispetto all'osso dovuto alla presenza di tessuti molli. Il metodo è stato convalidato su un braccio robotico e su 5 partecipanti sani mediante il confronto tra le IMU e, rispettivamente, gli encoder del robot e un sistema optoelettronico. Per il secondo obiettivo, è stato chiesto a 10 partecipanti sani di eseguire un insieme di attività in due scenari diversi: uno caratterizzato da attività semplici (SADL) e l'altro di attività complesse (CADL). Durante gli esperimenti, i dati sono stati acquisiti mediante 5 IMU e una videocamera. I dati sono stati etichettati mediante ispezione video in base alla definizione di 5 primitive motorie: "idle", "stabilize", "reach", "transport" e "reposition". Successivamente, è stata addestrata e testata una rete neurale LSTM (Long-Short Term Memory) con diverse combinazioni di dataset: SADL per addestramento e test, e SADL+CADL per addestramento e test. I risultati della validazione degli angoli ISB hanno mostrato un errore inferiore durante il test sul braccio robotico (RMSE medio tra 2,75°-4,96°) rispetto a quello sui partecipanti (RMSE medio tra 9,45°-29,65°). Tuttavia, il coefficiente di correlazione è stato superiore a 0,91 anche durante la convalida con soggetti sani. Per quanto riguarda le prestazioni della classificazione del modello LSTM sui due dataset, il primo ha ottenuto un f1-score di 0,75, mentre il secondo, che è più rilevante per l'applicazione finale, ha ottenuto uno score f1 di 0,73. L'algoritmo ha ottenuto migliori risultati nel riconoscimento delle primitive "idle" e "transport", che erano le più presenti nei dataset. Al contrario, le primitive "reach" e "reposition" sono state spesso classificate erroneamente come "transport". Questo lavoro rappresenta un punto di partenza per la valutazione degli arti superiori in scenari di vita quotidiana.

Parole chiave: cinematica degli arti superiori, controllo di exosuit, calcolo degli angoli articolari tramite IMU, standard ISB, classificazione delle primitive motorie, reti neurali